AGU PUBLICATIONS

JGR

Journal of Geophysical Research: Solid Earth

RESEARCH ARTICLE
10.1002/2017JB014261

Key Points:
- Absolute motions of stable Europe, Siberia and North China-Amuria since 260 Ma are reconstructed using paleomagnetic data
- Time-varying convergence rates disclose three stages during the closing of the Mongol-Okhotsk Ocean in the Mesozoic
- The genesis for the seismologically defined slab morphology underneath Eurasia is investigated from plate reconstructions

Supporting Information:
- Supporting Information S1

Correspondence to:
L. Wu,
lei.wu@ualberta.ca

Citation:
Wu, L., V. A. Kravchinsky, Y. J. Gu, and D. K. Potter (2017), Absolute reconstruction of the closing of the Mongol-Okhotsk Ocean in the Mesozoic elucidates the genesis of the slab geometry underneath Eurasia, *J. Geophys. Res. Solid Earth*, *122*, doi:10.1002/2017JB014261.

Received 3 FEB 2017
Accepted 28 JUN 2017
Accepted article online 3 JUL 2017

Absolute reconstruction of the closing of the Mongol-Okhotsk Ocean in the Mesozoic elucidates the genesis of the slab geometry underneath Eurasia

Lei Wu[1,2], Vadim A. Kravchinsky[1], Yu J. Gu[1], and David K. Potter[1]

[1]Department of Physics, University of Alberta, Edmonton, Alberta, Canada, [2]CAS Key Laboratory of Mineralogy and Metallogeny, Guangzhou Institute of Geochemistry, CAS, Guangzhou, China

Abstract Understanding the present-day fast seismic velocity anomalies in the mantle requires an accurate kinematic reconstruction of past convergent tectonics. Using the paleomagnetism-based absolute reconstruction method from Wu and Kravchinsky (2014), we present here the restoration of the closing of the Mongol-Okhotsk Ocean (MOO) that existed between Siberia and North China-Amuria (NCA) during the Mesozoic. Three stages, i.e., 250–200 Ma, 200–150 Ma, and 150–120 Ma, are identified from the time-varying convergence rates of Siberia and NCA. The spherical distance between the suture margins was reduced by approximately 66.7% at an average convergence rate of 8.8 ± 0.6 cm/yr during the first stage at 250–200 Ma, when approximately 62.5–76.1% of the slabs associated with the MOO lithosphere were formed primarily through intraoceanic convergence. In the second stage at 200–150 Ma, the spherical distance was reduced by another 21.1% with a convergence rate of 3.6 ± 0.3 cm/yr. During this stage, approximately 14.2–30.9% of the MOO slabs were formed and continental-oceanic convergence outpaced intraoceanic subduction. In the last stage at 150–120 Ma, the convergence rate dropped to approximately 0.4–0.6 cm/yr with the formation of approximately 4.6–9.8% slabs associated with the MOO lithosphere. The final closure of the remnant MOO basin could have been accomplished by 130–120 Ma, which explains the origin of the fast-velocity anomalies inside the restored continents at 120 Ma near the suture margins.

1. Introduction

Plate tectonic theory predicts the subduction of oceanic lithosphere at convergent plate boundaries. The resultant descending slabs [*van der Hilst and Kárason*, 1999], usually represented as fast-velocity perturbations in tomographic images, not only contribute to the thermal and density heterogeneities in the mantle but also shape the Earth's surface elevation [*Lithgow-Bertelloni and Silver*, 1998], the gravity field [*Richards and Hager*, 1984; *Panet et al.*, 2014], the topography of the Earth's interior layer boundaries [*Hager et al.*, 1985; *Ishii and Tromp*, 1999], and the mantle cooling history [*Lay et al.*, 2008]. No simple method, however, is widely accepted to quantitatively relate the present-day mantle downwelling structures with the time-evolving surface kinematic processes. There are four major difficulties: (1) significant differences in plate reconstructions predicted by various absolute plate motion (APM) models, (2) disagreements in the distribution of slabs in the mantle inferred from various seismic tomography models, (3) uncertainties in existing relative plate motion models for transferring rotations from one plate to another, and (4) the commonly applied but oversimplified assumption of vertical slab sinking in constructing the time scales for the mantle.

The Mongol-Okhotsk Ocean (MOO), previously bounded by Siberia and North China-Amuria (NCA) [*Enkin et al.*, 1992], was the northern part of the extinct superocean Panthalassa that surrounded the supercontinent Pangea during the Late Paleozoic [*van der Meer et al.*, 2010]. Over the past decades, our understanding of the kinematic and subduction history of the closing of the MOO has been advanced through a combination of geologic and paleomagnetic geodynamic approaches. Based on the geochronology and geochemistry of subduction-induced magmatism and ophiolites along the Mongol-Okhotsk suture, it has been suggested that the closing of the MOO was a long-lasting process that could extend from the Silurian [*Kurihara et al.*, 2009] to the Late Jurassic [e.g., *Tomurtogoo et al.*, 2005; *Chen et al.*, 2011] or to the Early Cretaceous [e.g., *Donskaya et al.*, 2013]. Similar estimates of the timing of final closure of the MOO (~155–120 Ma) have been provided in traditional paleomagnetic studies (no paleolongitude constraints), where the overlapped paleolatitudes of both the Siberian and NCA sides of the suture boundaries are interpreted as final closure of the

ancient oceanic basin [e.g., *Kravchinsky et al*., 2002a; *Van der Voo et al*., 2015; *Ren et al*., 2016]. Using paleomagnetic reconstructions, *Van der Voo et al*. [1999] interpret the fast seismic velocity anomalies in the lower 1000 km of the mantle beneath Siberia (nearly perpendicular to the present-day MOO suture) as the "MOO slab." With recent advances in tomographic imaging and global plate reconstructions, *Van der Voo et al*. [2015] further suggest the final closure of the MOO to be at 160–140 Ma by matching the paleolatitude-based reconstructions of Siberia and NCA with their identified downgoing lithosphere associated with the MOO [*van der Meer et al*., 2010].

Despite the advances, one main issue remains to be resolved regarding the presuturing kinematic evolution of the MOO, when little quantitative paleopositional constraints can be extracted from geologic observations on the paleolatitude-based reconstructions of Siberia and NCA. An associated issue involves the interpretation of the fast-velocity zone in the lower mantle beneath Eurasia, often dubbed as a "slab graveyard" extending from northeastern stable Europe to the western Pacific [*Van der Voo et al*., 1999], which is one of the well-resolved structures in seismic tomography models [e.g., *Trampert et al*., 2004]. Specifically, the question remains to be addressed regarding how past surface kinematic processes had contributed to the genesis of the seismologically constrained slab graveyard at depths greater than 1500 km. Using kinematic reconstructions as surface boundary conditions, a recent geodynamic analysis predicts more westerly MOO slabs than tomographic revelations and challenges the existing APM models that use the MOO slabs as anchor points for paleolongitude constraints [*Fritzell et al*., 2016]. The key to resolving the current issues both with restoring the style and timing of the closing of the MOO and with interpreting the morphology of the lower mantle anomalous structures is to reconstruct APMs of the bounding continents Siberia and NCA during the Mesozoic reliably and independently.

Hot spot reference frames are one of the well-established APM models, but they cannot predict plate motions before 130 Ma [*Müller et al*., 1993; *Doubrovine et al*., 2012] because few hot spot tracks older than the Early Cretaceous have been recognized. By establishing anchor points at certain ages to provide longitudinal constraints, through either deep mantle structures [*Burke and Torsvik*, 2004] or estimates of true polar wander (TPW) [*Mitchell et al*., 2012], paleomagnetism shows the potential to extend APM reconstructions beyond the hot spot records. Based on the quasi-stationary African assumption, for example, *Torsvik et al*. [2008] propose a hybrid model in which absolute motions of the major continents earlier than 130 Ma are restored by transferring the finite rotations of Africa using plate circuits. However, this approach is not effective in constraining the APMs of the (South)east Asian plates such as NCA due to no preservation of local plate circuits. In recent years, slabs derived from seismic observations are frequently used to refine the existing APM models [e.g., *van der Meer et al*., 2010]. However, no consensus has been reached on the standard approach to characterizing slabs from either contours of velocity [*van der Meer et al*., 2010] or temperature perturbations [*Shephard et al*., 2012]. It is also unclear how trench migrations [*Williams et al*., 2015], and variations of depth-dependent slab sinking rates in the mantle [*Butterworth et al*., 2014], would affect the restoration of ancient subduction zones for which existing polarity determinations are fairly subjective. Equivocalness results if slabs in the middle to lower mantle, which are represented in the form of velocity anomalies and interpreted initially based on plate reconstructions [e.g., *Anderson and Dziewonski*, 1984], are used to refine the existing APM models.

Here we apply a new paleomagnetism-based APM method, apparent polar wander path geometric parameterizations [*Wu and Kravchinsky*, 2014], to independently restore the absolute motions of Siberia and NCA that previously bounded the MOO. The reconstructed closing of the MOO is then integrated with the fast-velocity zone beneath Eurasia to examine the relationships between past plate motions and the present-day distribution of slabs beneath Eurasia according to several widely adopted seismic tomography models.

2. Overview of Previous Studies of APM Models and True Polar Wander

2.1. Kinematic History of Stable Europe Predicted From Different APM Models

Figures 1 and S1 in the supporting information show the comparison of the kinematic reconstructions of a reference point (10°E, 60°N) in stable Europe over the last 260 Myr according to several widely cited APM models (Table S1). These models include (1) the fixed hot spot frame in the coordinates of North America (M93: interpolated with an increment of 10 Myr at 0-130 Ma) [*Müller et al*., 1993], (2) the global moving hot spot frame in the coordinates of stable Europe (D12: 0–120 Ma) [*Doubrovine et al*., 2012], (3) the sinking

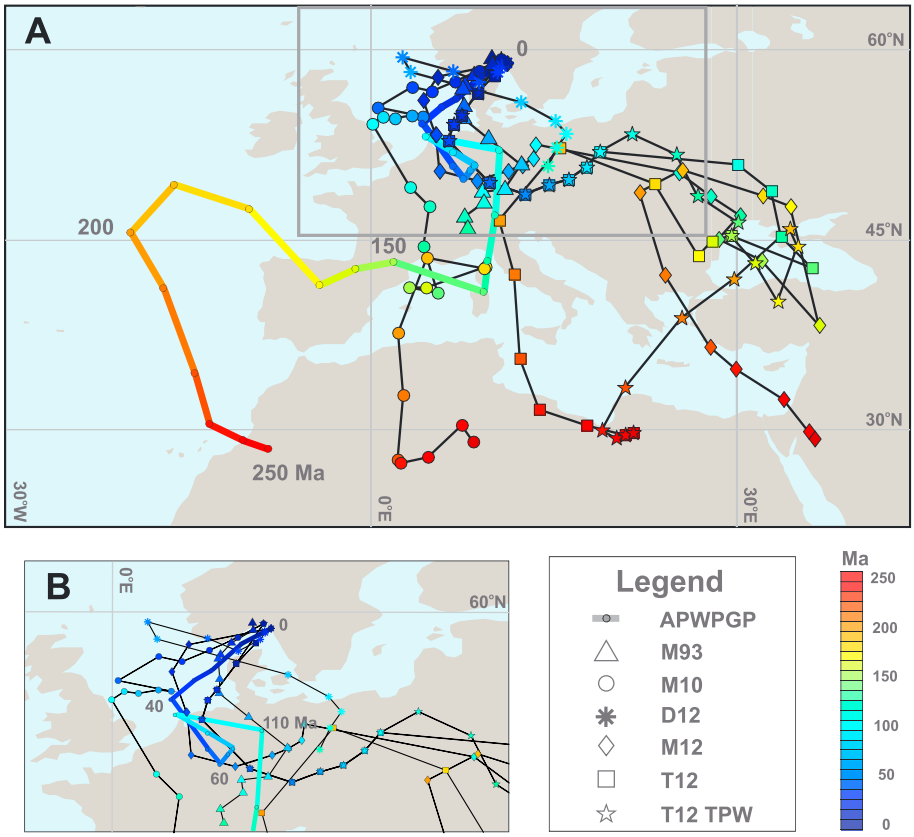

Figure 1. (a) Reconstructions of a reference site (10°E, 60°N) in stable Europe over the last 250 Myr according to different absolute plate motion (APM) models: M93 [*Müller et al.*, 1993], D12 [*Doubrovine et al.*, 2012], M10 [*van der Meer et al.*, 2010], M12 [*Mitchell et al.*, 2012], T12 [*Torsvik et al.*, 2012], T12-TPW [*Torsvik et al.*, 2012], and APWPGP from this work (see the text below for a detailed description of model construction). The reconstructions are color coded according to age. Different symbols represent predictions from different APM models. (b) Magnified area that is enclosed in the grey rectangle in Figure 1a.

slab frame in the coordinates of South Africa (M10: 0–260 Ma) [*van der Meer et al.*, 2010], (4) the paleomagnetism-based true polar wander (TPW) frame in the coordinates of stable Europe (M12: 0–260 Ma) [*Mitchell et al.*, 2012], (5) the global hybrid frame (a combination of hot spot and paleomagnetism-based frames) in the coordinates of South Africa (T12: 0–260 Ma) [*Torsvik et al.*, 2012], and (6) the TPW-corrected global hybrid frame in the coordinates of South Africa (T12-TPW: 0–260 Ma) [*Torsvik et al.*, 2012]. For the APM models not presented in the coordinates of stable Europe, (part of) the plate circuit of stable Europe-North America-Northwest Africa-South Africa is used to transfer the finite rotation parameters (Table S2) [*Torsvik et al.*, 2012].

Overall, all these APM models predict a northeastward motion of the reference point in stable Europe during the last 40 Myr (Figure 1). Comparable plate motion directions and velocities are predicted by two paleomagnetic frames T12 and T12-TPW (both in the same moving hot spot frame) until 60 Ma (Figures 1 and S1). Significant deviations arise among different APM model predictions at 70–130 Ma when high-quality determinations of hot spot traces and associated age progression become scarce. For ages earlier than 130 Ma, there are substantial discrepancies among the different APM model predictions (Figures 1 and S1). The discrepancies in the reconstructions can be attributed to (1) the adoption of different references, either the mantle [*Müller et al.*, 1993; *Doubrovine et al.*, 2012] or the Earth's spin axis [*Torsvik et al.*, 2012]; (2) uncertainties in the hot spot frames that arise from errors in the modeled hot spot motions; (3) errors propagated through transferring rotations using different plate circuits (with varying reliability); (4) uncertainties in the existing methods for slab characterization based on different tomography models and/or calculations of thermal structures in the mantle; (5) uncertainties in the TPW estimates; and (6) any combinations of the above. To a large degree, such differences accentuate

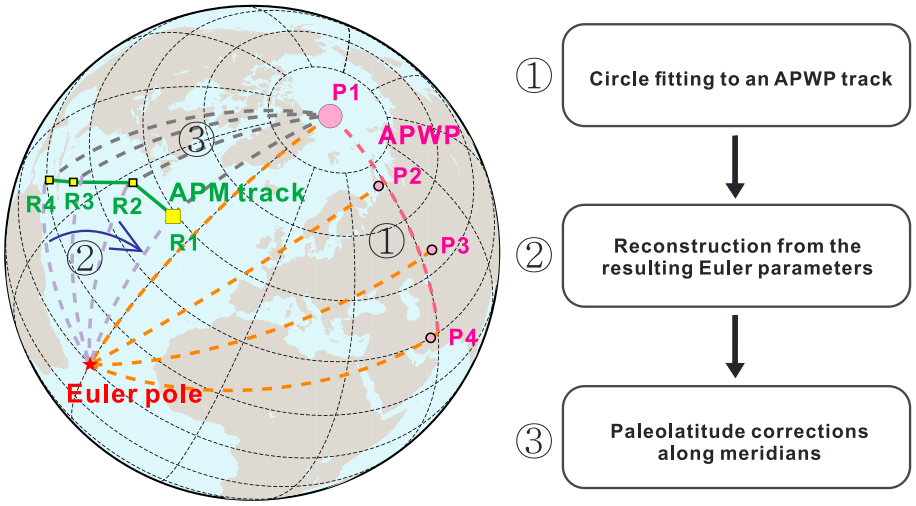

Figure 2. Flow chart showing the three-step procedure for deriving absolute plate motion (APM) by geometrically parameterizing a hypothetical apparent polar wander path (APWP) track. Stage Euler pole (red star) and the associated angle are computed by applying circle fits to the APWP track (P1–P4, where the present-day pole P1 coincides with the spin axis). The resulting APM track of a reference site R1 is calculated from the combination of Euler rotations and paleolatitude corrections. Paleolatitude corrections use paleocolatitudes as the spherical distances between the reconstructions (R1–R4) and the spin axis (P1).

the need for reliable APM reconstructions, especially those determined independently of hot spots and/or sinking slabs.

2.2. Apparent Polar Wander Path Geometric Parameterization Method

Figure 2 illustrates the three-step procedure for deriving APM by geometrically parameterizing a hypothetical apparent polar wander path (APWP) track [*Wu and Kravchinsky*, 2014]. Contrary to traditional paleomagnetic reconstructions where paleopoles from a given tectonic plate are individually restored to the spin axis, here we treat paleopoles as an integral sequence and investigate their spatial-temporal distribution for the kinematic implications. First, track fit with either great circle or small circle approach is applied to the identified APWP track to determine Euler pole and rotation angle. The resulting Euler rotation parameters are then adopted to calculate the absolute paleopositions of a given reference site at the same ages of the input paleopoles. The final reconstructions are determined by applying paleolatitude corrections to each of the restorations from the second step that are distributed along a circle arc. During the paleolatitude corrections, paleocolatitudes are adopted as the great circle distances between the spin axis and each of the final reconstructions. APM reconstructions from this methodology are with respect to a "fixed" space defined by the present-day spin axis and meridian of Greenwich (equivalent to the space defined by the fixed hot spots). Readers are referred to supporting information for the detailed formulation.

2.3. True Polar Wander

We follow the common definition that an apparent polar wander path (APWP) describes the motion of the Earth's spin axis with respect to a given lithospheric plate. APM is defined as the motion of the plate with respect to the space (equivalent to the one from the above method) that is defined by fixed hot spots [*Morgan*, 1971; *Müller et al*., 1993]. TPW is defined as the motion of the Earth's spin axis with respect to the same space [*Besse and Courtillot*, 2002; *Courtillot*, 2007; *Raub et al*., 2007]. The three terms of motions can be linked through the multiplication of rotation matrices (dot product).

$$\mathrm{APWP} = \mathrm{APM}\cdot\mathrm{TPW}$$

Long-term TPW events have been estimated from either the comparison of the paleomagnetic and hot spot-derived paleolatitudes of seamounts [e.g., *Tarduno and Gee*, 1995] or the differences between a paleomagnetic frame and a hot spot frame in the coordinates of the same plate [e.g., *Besse and Courtillot*, 2002; *Doubrovine et al*., 2012].

3. Methods

3.1. Paleomagnetic Data

The Siberian APWP used for the geometric parameterizations comprises two segments: the stable European running means for 0–240 Ma [*Torsvik et al*., 2012] and the Siberian running means for 250–260 Ma [*Cocks and Torsvik*, 2007]. The main segment of the North China APWP (60–230 Ma) is from *Van der Voo et al*. [2015], with our interpolations at 140, 200, and 230 Ma. The 240–260 Ma segment is calculated in a sliding window of 20 Myr using the freeware PMTec [*Wu et al*., 2015] from the selected high-quality North China paleopoles (with quality factors no smaller than 5, Table S3). For simplification, we assume that the Amuria Block accreted to the North China Block before 260 Ma based on their overlapped paleolatitudes on the suture [*Kravchinsky et al*., 2002b]. We also simplify the complexity that stable Europe and Siberia might not behave as a rigid single plate, as implied from their different paleopoles during the Mesozoic [*Metelkin et al*., 2010] or even during the Cenozoic [*Cogné et al*., 2013]. However, such nonrigidity does not critically change the first-order reconstructions of Siberia and NCA and their spatial relationships with the underlying slabs. We use the stable European running means of 0–50 Ma [*Torsvik et al*., 2012] as the first segment of the input North China APWP, mainly to avoid the confusion associated with the sparse and less certain North China paleopoles in the Cenozoic. To estimate errors in rotation parameters and associated reconstructions, a minimally acceptable error of 16.0° is assigned to the North China APWP poles that are interpolated or averaged from less than two input paleopoles. Table S4 tabulates the input APWPs for the geometric parameterizations.

3.2. Geometric Parameterization of the Apparent Polar Wander Paths

Both great circle (GC) and small circle (SC) approaches are implemented to derive stage Euler rotation parameters from the APWPs (see supporting information Text S1 for the detailed methods). GC fits present more conservative reconstructions because much lower polar/plate motion speeds are predicted from APWP tracks compared to their SC counterparts. Better circle fit options are determined by comparing the variance ratio V_r with the critical value $F_{1,n-3}$ at the 0.05 significance level [*Wu and Kravchinsky*, 2014] (see supporting information Text S1 for details).

Eight tracks (one track is a best fit circular segment to all paleopoles at a given interval) are identified from the Siberian (and stable European) APWPs (Figure 3a and Table S5). There are other options for fitting the segment of 60–110 Ma, to which we apply a single circle fit considering the statistically insignificant differences between the paleopoles at the interval. Paleolatitude corrections are then applied to the reconstructions to correct errors associated with the imperfectly circular distribution of paleopoles along the best fit tracks. This is achieved by using paleocolatitudes determined from paleomagnetism as the spherical distances between the spin axis and the reconstructions of a given reference site, rather than keeping all restorations along the circular tracks centering on stage Euler poles [*Wu and Kravchinsky*, 2014; *Wu et al*., 2015]. In the same way, the identified North China APWP segments are fitted with both great and small circles (Figures 3 and 4). Other combinations of circle track fits for the paleopoles with heavily overlapped errors at 40–150 Ma have been tested without significantly changing the resulting reconstructions.

The stage and finite Euler rotations are listed in Tables S6 and 1, with the resulting reconstruction shown in Figures 5 and 6 (see section 5 for a detailed discussion). Error ellipses for the rotation poles and associated reconstructions are expressed as the primary axes (i.e., semimajor and semiminor) and the angle from the meridian to the right-hand semimajor axis. These parameters are derived from the symmetric uncertainty covariance matrices defined by *Wu and Kravchinsky* [2014]. To investigate how Siberia and NCA have moved relative to the mantle during the last 260 Myr, we correct the motion of the spin axis from our APM reconstructions by adding the finite rotations of the TPW events identified by *Torsvik et al*. [2012, Table 12] (the data are based on an earlier study by *Steinberger and Torsvik* [2008]). For the sake of comparison, we then apply the same TPW corrections to the APWPs of Siberia and North China before circle fits to assess how different the resulting reconstructions are compared to those acquired from the above procedures.

3.3. Slab Characterization

To characterize slabs in the lower mantle beneath Eurasia, we adopt two *P* velocity global tomography models MIT-P (0.2 ± 0.1%) [*Li et al*., 2008] and GAP-P4 (0.3 ± 0.1%) [*Obayashi et al*., 2013], because (1) *P* velocity models based on automatically determined travel time data (e.g., data from the Bulletin of the International Seismological Centre) are resistant to phase picking errors (Y. Fukao, personal

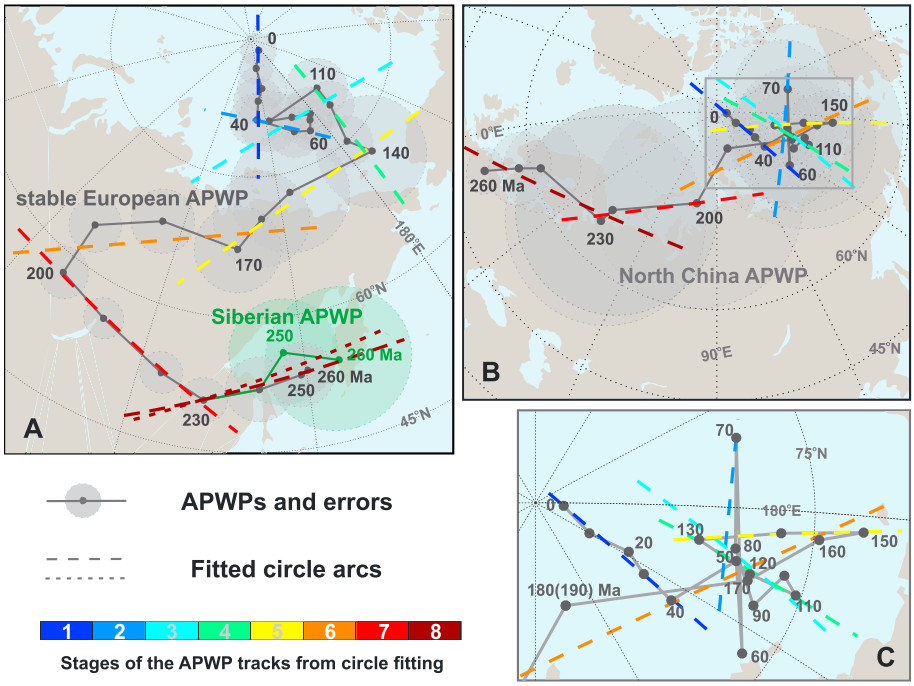

Figure 3. Circle fits (dashed lines color coded according to different stages) to the identified tracks of the apparent polar wander paths (APWPs) of stable Europe, Siberia, and North China over the last 260 Myr (Table S4) for the derivation of their stage Euler rotations (Table S6). Errors in the input paleopoles are shown in the single colored circles. (a) Great circle fits to both the EU (dark grey dots and connecting line) and Siberian (green dots and connecting line) APWPs during eight stages: 0–40 Ma, 40–60 Ma, 60–110 Ma, 110–140 Ma, 140–170 Ma, 170–200 Ma, 200–230 Ma, and 230–260 Ma (Tables S5 and S6). The circle fit to the eighth APWP track of Siberia is distinguished from that of EU with a short dashed line. (b) Circle fits to the North China APWP during eight stages: 0–40 Ma, 40–80 Ma, 80–110 Ma, 110–130 Ma, 130–150 Ma, 150–200 Ma, 200–230 Ma, and 230–260 Ma (Tables S5 and S6). (c) Magnified area that is enclosed in the grey rectangle in Figure 3b. Small circle fits and errors in the paleopoles are not shown for clarity.

communication, 2016), and (2) the two models include data from local stations and show intermodel consistency in the inferred mantle structure (W. Spakman, personal communication, 2017). For comparison, we adopt two *S* velocity models: S40RTS (0.6 ± 0.1%) [*Ritsema et al*., 2011] and s10mean (0.6 ± 0.1%) that is averaged from a variety of global *S* velocity models [*Doubrovine et al*., 2016].

We adopt 3-D contours of *X*% velocity perturbation (*X* is the percentage velocity perturbation from a given tomography model) to represent slabs, whose uncertainties are approximated by the fast velocity anomalies encompassed in the $X \pm 0.1\%$ contours. Such uncertainties, however, do not significantly affect the discontinuous long-wavelength velocity structures associated with slabs. The values of percentage velocity perturbation for MIT-P and S40RTS are determined by *Butterworth et al*. [2014], who apply an iterative dynamic approach for slab characterization. The values of velocity perturbations for the remaining tomography models are selected such that location and volume of these isosurfaces are comparable among different models. We note that the suggested velocity contours might include the ambient mantle that is thermally disturbed by sinking slabs.

3.4. Linking Past Plate Kinematics With Penetrative Convection

To decipher the correlation between past plate kinematics and slab distribution, we first calculate the time-dependent velocity vectors of three reference sites on the MOO suture (i.e., Ref-1, Ref-2, and Ref-3 from Figure 5a) using the rotation parameters of Siberia and NCA (Table 1). Great circle distances between the same references at both the Siberian and NCA sides of the suture are calculated as proxies for the size of the downsizing MOO oceanic basin. The rates of convergence between the two continents and associated ranges are then computed as the slopes of the time-varying spherical distances (Figure 7). Note that convergence rates remain the same before and after TPW corrections.

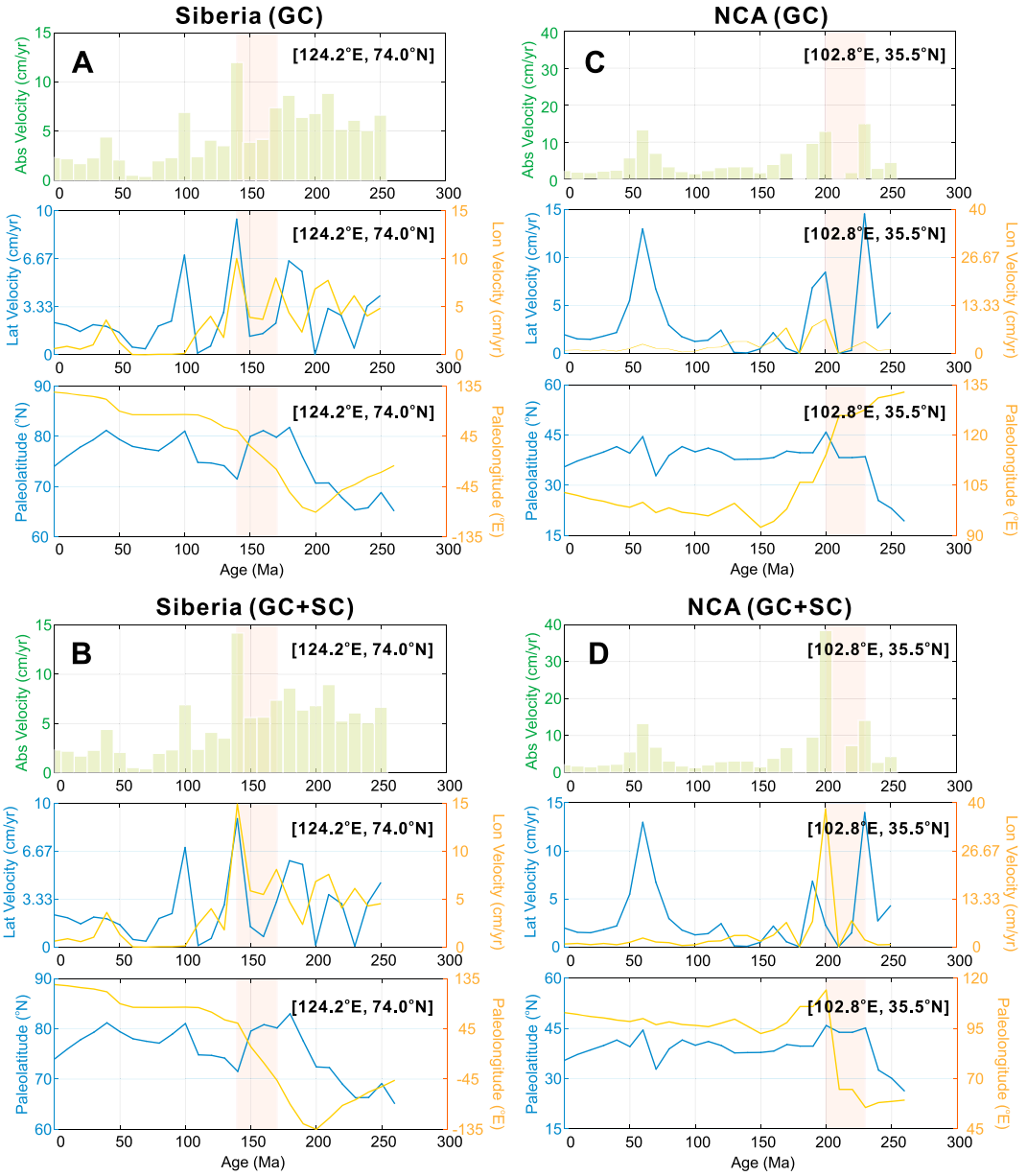

Figure 4. Comparison of alternative circle fit approaches to the Siberian and North China APWPs. (a) Kinematic predictions exclusively from the great circle (GC) fits. Reconstructions are calculated in the coordinates of a reference site (124.2.0°E, 74.0°N), which is located approximately at the center of the Siberian plate polygon. (b) Kinematic reconstructions of the same reference site from a combined GC and small circle (SC) fits. (c and d) Same as in Figures 4a and 4b but in the coordinates of a reference site (102.8°E, 35.5°N) from NCA. Pink shadings highlight the intervals where the SC approach is better the GC method on circle fitting to the identified APWP segments (Table S5).

To quantify the time-dependent production of slabs associated with the closing of the MOO, we compute two parts of area enclosed in $X \pm 0.1\%$ velocity contours (X is the percentage velocity perturbation from a given tomography model; see section 3.3). The first part of intersection is related to intraoceanic subduction of the MOO, which is approximated from the area of intersections between a closed polygon representing the MOO basin at a given age and $X \pm 0.1\%$ velocity contours at the corresponding depth (Table S10). The second part of slabs is associated with continental-oceanic subduction of the MOO (with possible minor contributions from the subduction of edges of the Tethys and Panthalassa), which is computed from the area of intersection between reconstructed plate polygons

Journal of Geophysical Research: Solid Earth
10.1002/2017JB014261

Table 1. Finite Reconstruction Parameters for Siberia, Stable Europe, and North China for the Last 260 Myr

	Finite Rotations of Siberia									Finite Rotations of North China-Amuria								
	Original		TPW Corrected				Error Ellipses			Original		TPW Corrected				Error Ellipses		
Age (Ma)	Longitude (°E)	Latitude (°N)	Angle (deg)	Longitude (°E)	Latitude (°N)	Angle (deg)	Maj (deg)	Min (deg)	Az (deg)	Longitude (°E)	Latitude (°N)	Angle (deg)	Longtude (°E)	Latitude (°N)	Angle (deg)	Maj (deg)	Min (deg)	Az (deg)
0	0.0	0.0	0.0	0.0	0.0	0.0	0.0	0.0	90.0	0.0	0.0	0.0	0.0	0.0	0.0	0.0	0.0	90.0
10	48.1	0.9	2.1	48.1	0.9	2.1	3.4	2.0	−76.8	48.1	0.9	2.1	48.1	0.9	2.1	2.3	0.8	−19.2
20	51.3	0.7	4.1	51.3	0.7	4.1	3.8	2.5	−83.7	51.3	0.7	4.1	51.3	0.7	4.1	2.5	1.8	−33.4
30	49.8	0.8	5.6	49.8	0.8	5.6	4.1	2.8	89.4	49.8	0.8	5.6	49.8	0.8	5.6	2.7	2.3	−55.1
40	49.5	0.8	7.7	49.5	0.8	7.7	4.4	3.0	−89.1	49.5	0.8	7.7	49.5	0.8	7.7	3.3	2.6	67.2
50	73.5	−1.3	9.5	73.5	−1.2	9.5	2.9	2.5	44.1	62.6	−1.2	7.1	62.6	−1.2	7.1	4.3	2.7	84.6
60	82.9	−2.2	10.5	82.9	2.6	10.5	2.7	2.3	−82.7	35.2	2.6	10.4	35.2	2.6	10.4	6.8	3.6	55.0
70	87.0	−2.5	10.4	87.0	−7.4	10.4	3.3	2.5	−65.8	118.2	−7.4	7.8	118.2	−7.4	7.8	7.2	6.5	46.9
80	89.7	−2.8	10.5	89.7	−2.0	10.5	3.7	2.8	−83.5	68.0	−2.0	6.9	68.0	−2.0	6.9	6.0	3.8	52.0
90	80.8	−2.1	10.3	80.8	0.2	10.3	4.4	2.4	−74.1	61.3	0.2	9.5	61.3	0.2	9.5	9.0	4.6	84.6
100	70.0	−1.3	10.4	70.0	−1.2	10.4	6.9	3.2	−79.5	70.0	−1.2	9.0	70.0	−1.2	9.0	13.3	8.5	76.0
110	103.7	−3.9	11.0	66.9	−3.7	13.3	6.5	3.3	88.5	66.5	−0.5	10.2	42.4	−2.4	16.2	8.9	3.7	87.8
120	96.7	−2.6	13.2	66.7	−4.2	15.9	6.1	2.8	86.7	66.3	−1.1	7.7	38.0	−2.4	13.9	9.0	3.6	−81.9
130	91.7	−1.3	17.3	68.6	−6.6	20.2	6.2	2.7	82.2	71.9	−3.8	4.4	31.6	−2.9	10.8	9.7	5.4	−86.9
140	95.8	−1.6	19.8	74.6	−6.2	22.0	6.7	5.1	73.0	84.7	−2.9	8.6	49.4	−4.4	13.3	16.9	12.1	82.6
150	67.0	1.9	20.8	67.0	−2.5	20.8	9.5	5.0	−71.9	87.9	−2.5	13.1	87.9	−2.5	13.1	11.2	4.8	89.6
160	57.0	3.1	22.5	66.4	−0.9	19.7	9.0	4.6	−85.6	84.6	−2.4	11.0	108.4	−0.2	10.6	10.9	4.2	88.3
170	48.9	3.9	24.7	66.0	3.5	18.5	9.3	4.5	82.9	63.5	−0.1	7.7	136.5	3.5	7.5	14.8	7.0	83.8
180	34.5	6.5	24.0	58.1	18.0	13.0	10.8	3.9	83.6	−28.8	7.0	5.6	−147.4	1.5	9.9	9.9	3.3	−74.8
190	16.1	9.4	27.2	22.7	21.8	9.8	13.0	3.8	83.2	−28.8	7.0	5.6	−154.1	0.5	14.2	9.9	3.1	−73.8
200	14.7	7.4	33.5	19.1	16.6	11.4	13.1	4.0	80.9	−28.7	5.0	15.0	−127.8	−2.3	14.6	17.5	13.6	−77.2
210	24.1	4.5	34.8	35.0	18.4	18.0	9.2	3.6	73.8	−59.5	7.6	25.1	−100.7	−0.9	25.5	16.6	12.2	−50.5
220	35.6	0.7	37.6	46.6	14.9	26.1	6.9	3.1	63.4	−59.5	7.6	25.1	−90.9	1.3	24.2	15.6	11.6	−41.4
230	42.5	−1.7	40.4	49.8	11.8	33.1	5.9	3.4	60.4	−59.4	7.4	26.6	−79.0	3.4	25.0	15.8	12.9	−66.5
240	50.9	−4.6	38.4	55.2	11.7	35.1	6.0	4.2	73.7	−77.3	9.3	36.0	−84.3	7.0	36.1	9.5	6.4	−48.7
250	54.6	−5.9	37.3	54.6	−5.9	37.3	8.1	5.8	−80.8	−80.2	9.5	38.6	−80.2	9.5	38.6	8.0	5.7	−51.7
260	64.0	−8.9	36.8	64.0	−8.9	36.8	7.7	6.9	67.1	−84.1	9.7	43.1	−84.1	9.7	43.1	7.1	5.5	−52.3
Stable Europe																		
240	50.8	−4.6	38.7	55.1	11.7	35.4	5.9	4.2	73.5									
250	57.5	−6.9	37.9	57.5	−6.9	37.9	5.7	4.2	67.4									
260	58.6	−7.2	37.8	58.6	−7.2	37.8	5.3	3.2	64.5									

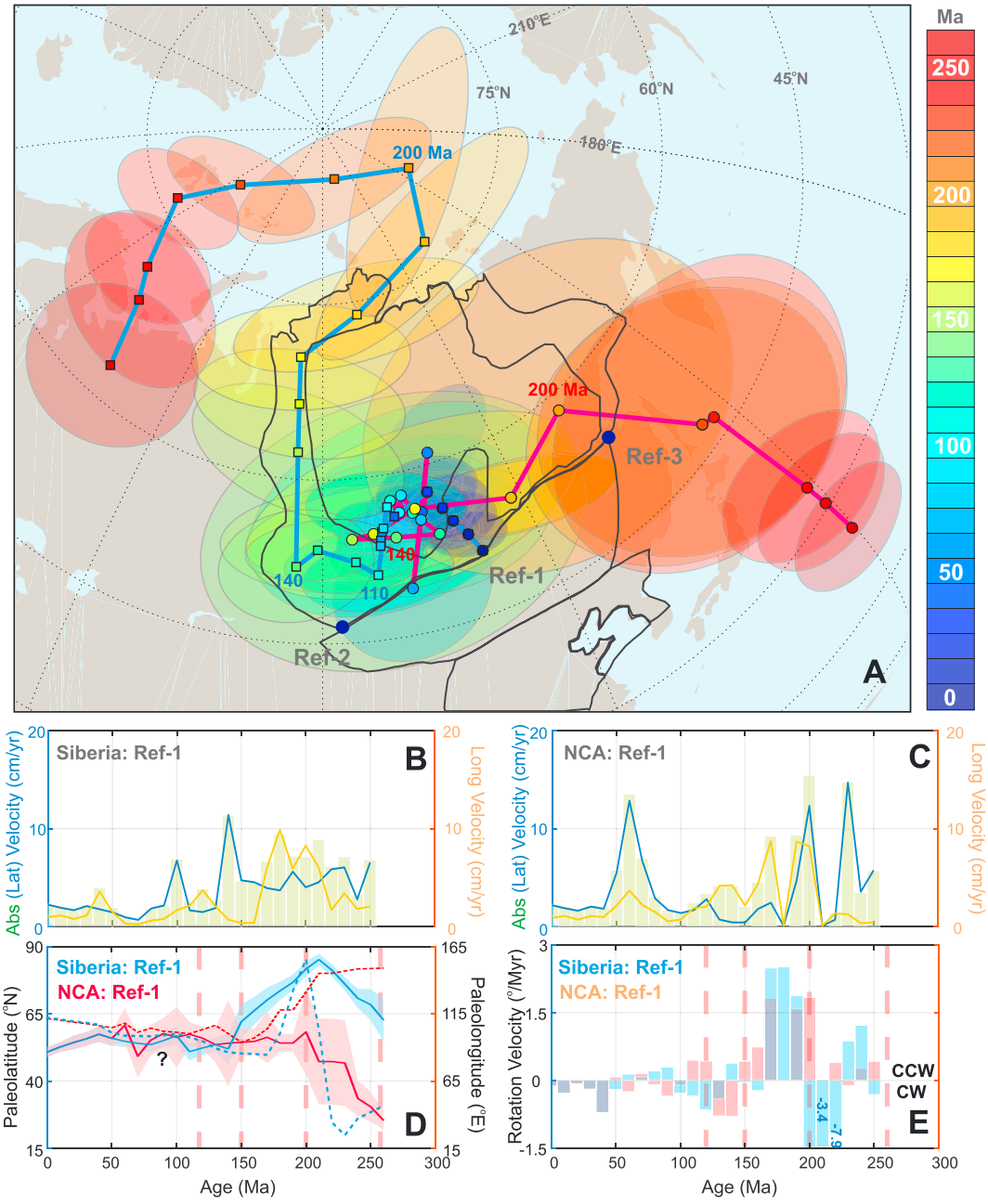

Figure 5. Absolute kinematic reconstructions of Siberia and North China-Amuria (NCA) since 260 Ma from the APWPGP method. (a) Restorations of reference point Ref-1 (112.0°E, 51.0°N) to delineate the motion trajectories of NCA (circles with the red connecting line) and Siberia (squares with the blue connecting line). Present-day locations of the two continents are shown as the grey contours for reference. Reconstruction errors are shown as the color-coded ellipses. Ref-1, Ref-2, and Ref-3 (Ref-2 and Ref-3 are located in the two ends of the suture) are used to calculate the time-dependent convergence rates of the suture boundaries (Figure 7). (b and c) Absolute velocities (green bars) along with latitudinal and longitudinal components (blue and orange solid lines) of the two continents in the coordinates of Ref-1. (d) Paleolatitudinal (solid lines) and paleolongitudinal (dashed lines) motions of Siberia (blue) and NCA (red). Error bounds in paleolatitudes and paleolongitudes from the APWPGP method are not shown due to their nonaxially symmetric shapes (Table 1). Instead, the simplified error bounds in paleolatitudes (blue and red shadings) are from uncertainties of paleopoles. The question mark indicates anomalous reconstructions due to imperfect paleomagnetic data. (e) Rotation rates of Siberia (blue bars) and NCA (red bars) in the coordinates of Ref-1. The vertical dashed lines in Figures 5d and 5e highlight the three stages during the closing of the Mongol-Okhotsk Ocean (MOO).

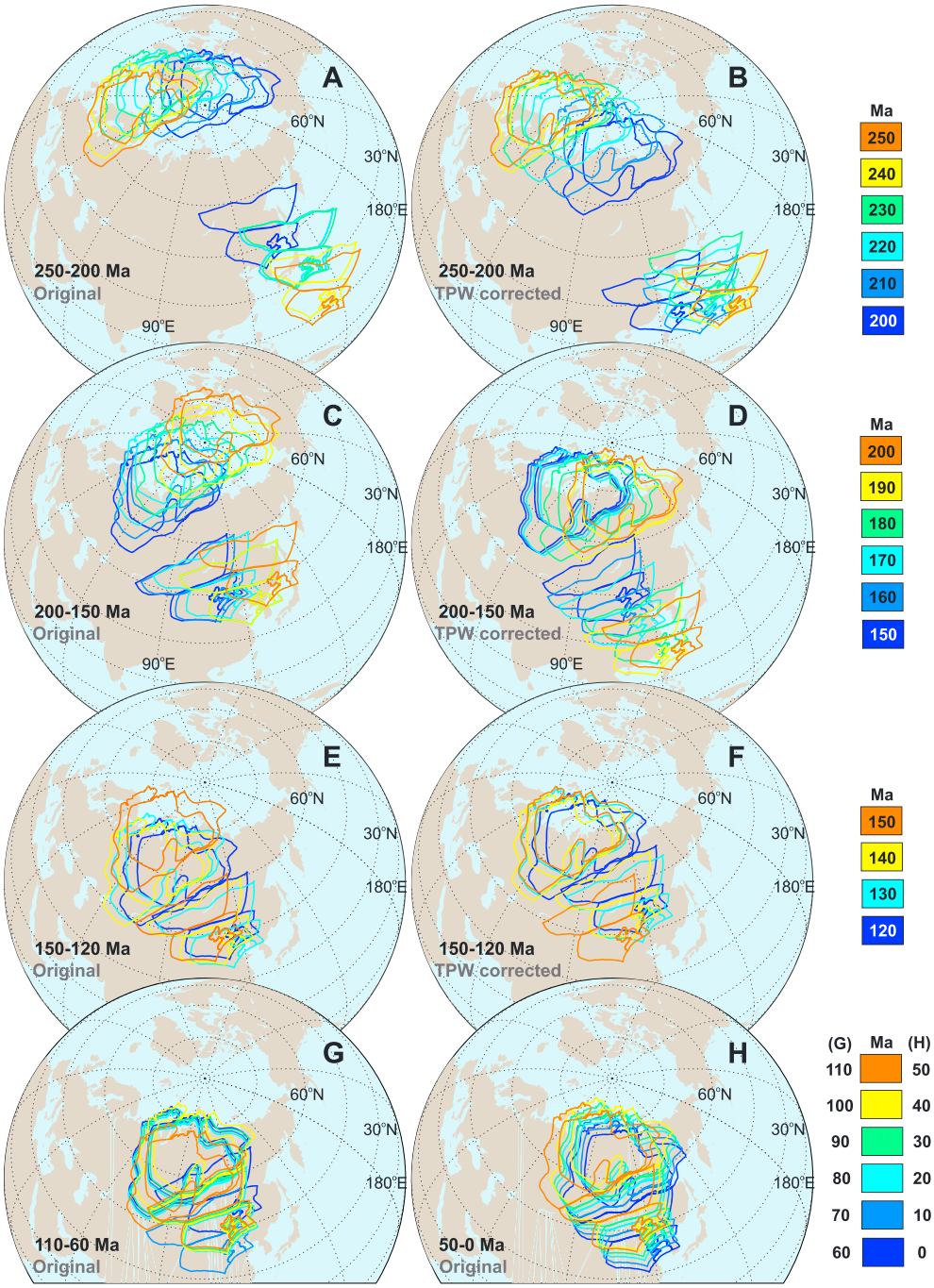

Figure 6. (a–f) Absolute reconstructions of Siberia and NCA since 250 Ma. Reconstructions on the left (right) column are with respect to the present-day spin axis (the mantle). (g and h) Absolute reconstructions of Siberia and NCA since 110 Ma with respect to the spin axis. There are postsuturing anomalies in the reconstructed Siberia and NCA at 60 (overlap), 70 (gap), and 110 (overlap) Ma, which result from the imperfect European and North China paleopoles at those ages.

and $X \pm 0.1\%$ velocity contours. For example, a polygon representing the MOO basin at 250 Ma is constructed with the restored suture boundaries of Siberia and NCA and two connecting great circle arcs (Figure 8). Rather than inferring the locations of paleotrenches from individual tomographic models, we use great circle arcs to approximate the boundaries between different paleooceans (e.g., between the MOO and Panthalassa) such that the constructed MOO polygons do not depend on the tomographic models. From the *P* velocity model GAP-P4, the total production of slabs related to both

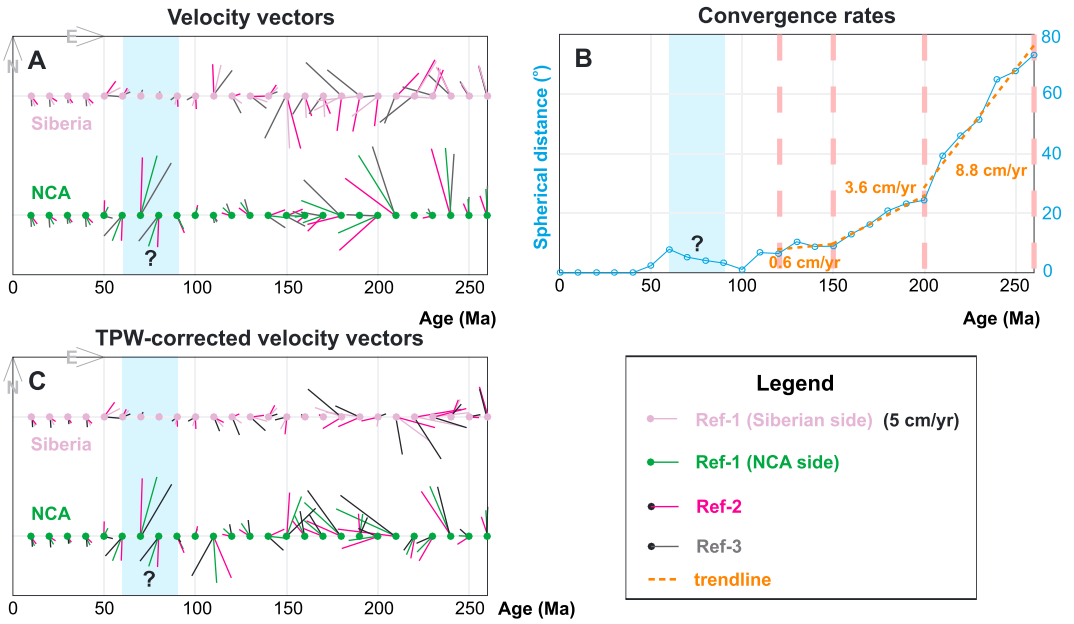

Figure 7. (a) Time-dependent absolute velocity vectors of the reference sites (Ref-1 (112.0°E, 51.0°N) in green and light purple, Ref-2 (105.1°E, 41.8°N) in magenta, and Ref-3 (135.4°E, 53.7°N) in grey, see the legend) along the suture boundaries relative to the spin axis. (b) The time-dependent spherical distances (blue dots and connecting line) between the suture boundaries in the coordinates of Ref-1. Convergence speeds of the suture boundaries are calculated as slopes of the best fit trendlines (orange dashed lines) of the spherical distances. Ranges for the slopes are determined from the time-varying spherical distances calculated in the coordinates of Ref-2 and Ref-3 (Figure 5a). The resulting convergence rates and associated ranges are 8.8 [8.2, 9.3] cm/yr at 260–200 Ma, 3.6 [3.4, 3.9] cm/yr at 200–150 Ma, and 0.6 [0.4, 0.6] cm/yr at 150–120 Ma. Blue shadings with question marks show the postsuturing reconstruction discrepancies as the result of the input paleopoles. (c) Velocity vectors that are calculated in the coordinates of the same reference sites but relative to the mantle. Convergence rates remain the same regardless of TPW corrections.

intraoceanic and continental-oceanic subduction of the MOO at 250 Ma is approximated from the combined area of the purple and blue shadings. This procedure is then repeated to compute the MOO slab areas between the depths of 1200 km and 2800 km (Figures 9–11). We assume that velocity contour areas approximate the sinking and folded slabs beneath Eurasia that primarily result

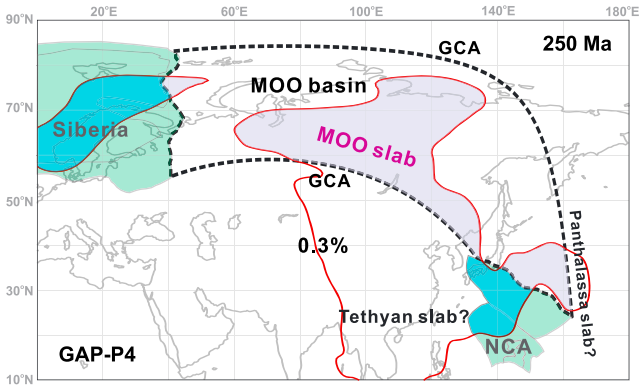

Figure 8. Schematic diagram of computing the depth-varying slab areas associated with the subduction of the MOO. For example, the MOO basin at 250 Ma is represented as a closed polygon (black dashed line) that is composed of the reconstructed Siberian and NCA sides of the suture and two connecting great circle arcs (GCAs). Area of the slabs associated with intraoceanic subduction of the MOO at the time (purple shadings) is determined from the intersections between the MOO basin polygon and the 0.3% velocity perturbation contours at the depth of 2733 km (red lines) from the *P* velocity model GAP-P4 [*Obayashi et al.*, 2013]. Similarly, area of slabs at the same depth associate with continental-oceanic subduction of the MOO is determined from the intersections (blue shadings) between the reconstructed plate polygons and the velocity perturbation contours.

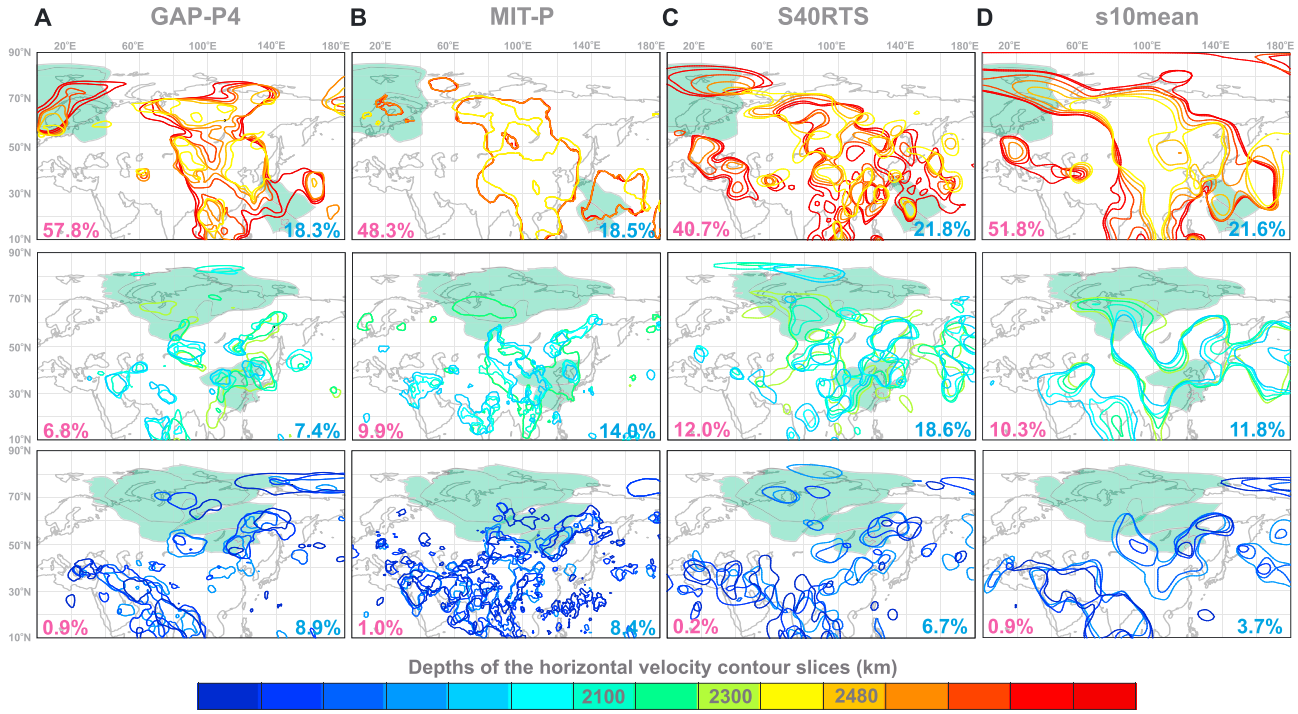

Figure 9. Slab distribution in the lower mantle beneath Eurasia according to various global tomography models: (a) 0.3% velocity perturbation contours from the *P* velocity model GAP-P4 [*Obayashi et al*., 2013], (b) 0.2% velocity perturbation contours from the *P* velocity model MIT-P [*Li et al*., 2008], (c) 0.6% velocity perturbation contours from the *S* velocity model S40RTS [*Ritsema et al*., 2011], and (d) 0.6% velocity perturbation contours from the *S* velocity model s10mean [*Doubrovine et al*., 2016]. The top row shows the horizontal velocity contour slices at the depths of 2800–2392 km with reconstructions at 250 Ma, the middle row shows velocity contour slices at the depths of 2300–1900 km with reconstructions at 180 Ma, and the bottom row shows velocity contour slices at the depths of 1819–1325 km with reconstructions at 120 Ma. Reconstructions with the TPW corrections are shown as the green shadings. Value in purple (blue) font in the lower left (right) corner of each plot is the percentage cumulative area of the MOO slabs associated with intraoceanic (continental-oceanic) subduction at the specified depth interval. Values are rounded to the thousandth digit for clarity.

from the downgoing Mongol-Okhotsk lithosphere possibly with minor contributions from the edges of Tethys and Panthalassa.

We follow the suggestions of *van der Meer et al*. [2010] to assign a time scale to different depths in the lower mantle (Table S10 and Figures 9–11). This time scale, primarily derived from the slab sinking rates of the MOO, Farallon, and Aegean Tethys slabs in the mantle [*van der Meer et al*., 2010], may not apply to slabs elsewhere when slab stagnation occurs (or occurred) in the transition zone [*Butterworth et al*., 2014; *Simmons et al*., 2015]. However, it is robust for relating the depth-dependent variations in slab areas with the plate kinematics during the closing of the MOO.

4. Circle Fits to the Siberian and North China APWPs

We compare circle fits using both the GC and SC approaches to the identified APWP segments (Table S5). The GC approach presents better fits to the majority of the APWP segments at the 0.05 significance level except the 170–140 Ma segment of the Siberian APWP and the 230–200 Ma segment of the North China APWP. Overall, GC fits lead to more conservative reconstructions because they predict much smaller rotation angles and associated polar/plate motion rates than their SC counterparts from the same APWP tracks (Table S5). For example, the GC fit to the 170–140 Ma segment of the Siberian APWP predicts a longitudinal rate of approximately 10 cm/yr at 150–140 Ma for a reference site (124.2°E, 74.0°N), while the SC fit predicts approximately 15 cm/yr (Figures 4a and 4b). Similarly, the GC fit to the 230–200 Ma segment of the North China APWP predicts an absolute velocity of approximately 13 cm/yr at 210–200 Ma in the coordinates of a reference site (102.8°E, 35.5°N), while the SC fit predicts an unreasonably high motion speed of approximately 38 cm/yr (Figures 4c and 4d). The two reference sites are the centroids of the Siberian and NCA polygons and can reasonably approximate the mean kinematics of the two plates.

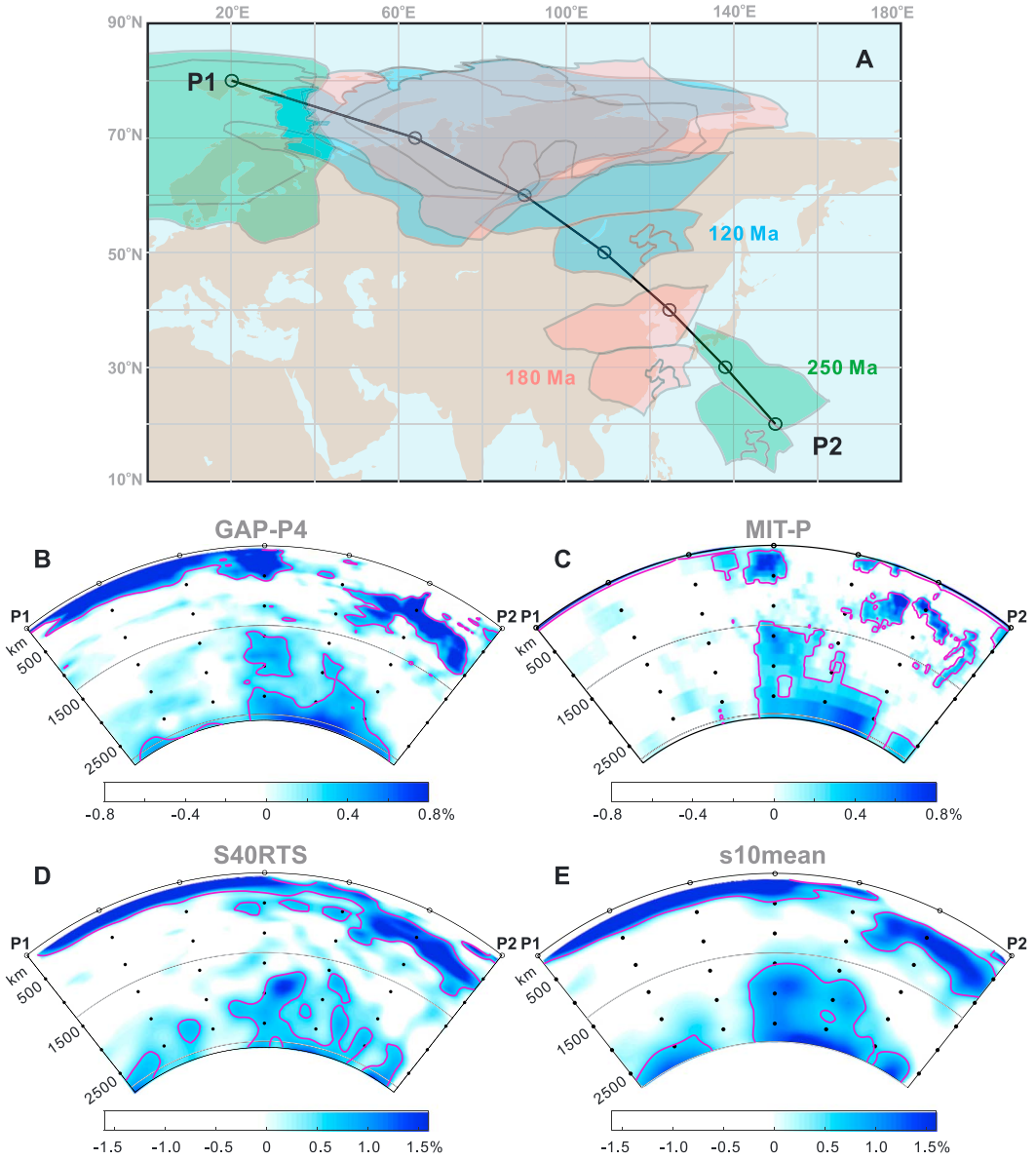

Figure 10. Vertical cross sections from various tomography models. (a) Map showing the TPW-corrected reconstructions at 250 Ma (green shadings), 180 Ma (pink shadings) and 120 Ma (blue shadings). The black line and circles denote the surface location of the vertical cross section (P1-P2). (b–e) Vertical cross sections from different tomographic models. Purple contours denote the *X*% velocity perturbations (see section 3). Grey lines show the depth range of 1325–2800 km for the horizontal velocity contour slices in Figure 9.

As shown in Figure 4, the GC and SC approaches present very different stage rotations and plate reconstructions. In our case, the SC fit to the 170–140 Ma segment of the Siberian APWP predicts more westward pre-170 Ma locations than its GC counterpart (Figures 4a and 4b). The SC fit to the 230–200 Ma segment of the North China APWP restores the pre-200 Ma locations of NCA west of its present-day location, opposite to the reconstructions exclusively from the GC fits (Figures 4c and 4d).

One may wonder why older stage rotations acquired from the GC approach are located close to the equator. This is because the apparent polar wander path geometric parameterization (APWPGP) approach is based on the assumption that it is plates, rather the spin axis, that have moved in geological history. We derive stage rotations from rotating all paleopoles back to the Earth's spin axis by assuming no TPW effects (they are then corrected from the resulting restorations). Specifically, the approach computes the stage rotation Si at the

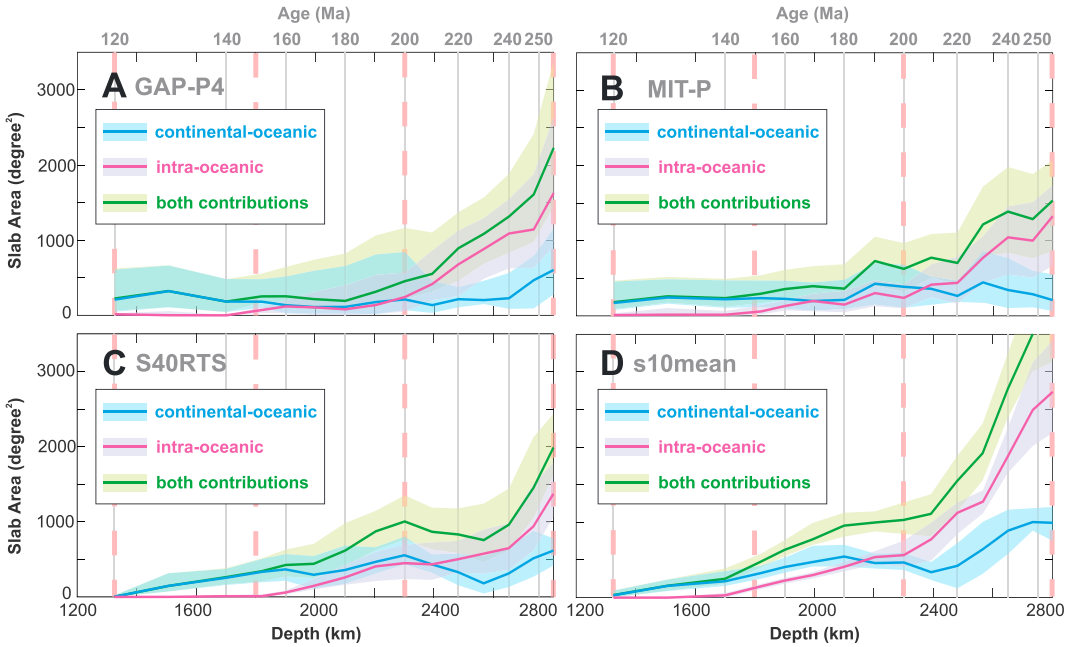

Figure 11. Depth-varying slab area associated with intraoceanic (purple) and continental-oceanic (blue) subduction of the MOO predicted from various tomography models (Figure 9). Uncertainties are approximated by the areas enclosed in the $X \pm 0.1\%$ contours, where X is the percentage of velocity perturbation (see section 3). The relation between depths and reconstruction ages is established following *van der Meer et al.* [2010]. Pink dashed lines in each plot indicate the three stages during the closing of the MOO identified from our kinematic reconstructions (Figure 7).

interval of i Ma by combining younger rotations (i.e., circle fits that are presented as $R_{i-1}, R_{i-2}, \ldots, R_1$) using matrix multiplication.

$$S_i = R_{i-1} \cdot R_{i-2} \cdot \ldots \cdot R_1$$

The equation shows that stage Euler poles acquired from the GC approach should be located close to the equator such that paleopoles from all APWP segments can be rotated back to the spin axis. This procedure can also be expressed in the form of matrix multiplication:

$$X_i^S = S_{i-1} \cdot S_{i-2} \cdot \ldots \cdot X_1$$

where X_i^S denotes a rotated paleopole that coincides with the spin axis or a reconstruction at the interval of i Ma.

One may expect that a SC fit predicts equally accurate or even better plate motions compared to its GC counterpart, which is a special case of the SC fit where the circle centre (i.e., Euler pole) is located at a great circle distance of 90° away from an APWP segment. This expectation is based on the observation that plates tend to move along SC arcs centering on Euler poles. One example is arc-shaped trajectories of seafloor spreading that are accommodated by displacement along fracture zones. However, GC fits do not necessarily predict plate motions along GC arcs because the kinematics of plate motions are also a function of the distances between a given plate and its Euler poles. By this logic, SC fits produce neither plate motions along SC arcs nor sensible reconstructions. Additional factors preventing accurate reconstructions from SC fits include (1) limited accuracy of existing paleopoles and/or APWPs and 2) constant plate rotations during certain time intervals.

5. Kinematic Reconstructions of Siberia and North China-Amuria Since 260 Ma

Figure 5a shows our restored absolute motions of Siberia and NCA in the coordinates of a reference site on the Mongol-Okhotsk Suture (Ref-1: (112°E, 51°N)). Depending on the distances to the rotation poles, velocities of different reference points on the same plate can vary significantly. Figures 5b–5e show the time-dependent kinematics of the suture boundaries of Siberia and NCA in the coordinates of Ref-1.

Three stages are disclosed: (1) 260–200 Ma when the Siberian side of the boundary went north rapidly (~6 cm/yr) to the near-polar region where it swung eastward (~140°) after a transition from a counterclockwise to clockwise rotation at 220 Ma, while the NCA side drifted as much as ~30° to approximately the present-day latitude during an overall counterclockwise rotation; (2) 200–150 Ma in which the Siberian side moved rapidly to the southwest at high latitudes with a predominantly counterclockwise rotation (~2.5°/Myr), while the NCA side drifted westward (~50°) with a counterclockwise rotation at an average rate of ~1.5°/Myr; and (3) 120–0 Ma when both the Siberian and NCA sides of the suture boundaries had a mostly eastward translation (~20°) after their suturing at 150–120 Ma. For completeness, Figure 1 shows the comparison between our reconstructions of the reference site (10°E, 60°N) in stable Europe and those determined from other APM models. Potential reasons for the differences are discussed in section 2.1.

To investigate how Siberia and NCA have moved relative to the mantle over the last 260 Myr, we correct our reconstructions using four TPW events identified by *Torsvik et al*. [2012]. These TPW events include (1) a counterclockwise (CCW) rotation of 22.5° at 250–200 Ma, (2) a clockwise (CW) rotation of 22.5° at 200–150 Ma, (3) a CW rotation of 8° at 150–140 Ma, and (4) a CCW rotation of 8° at 110–100 Ma around their identified "continental mass center" (11°E, 0°N). After removing the CCW rotation of the "whole Earth" (or the spin axis) at 250–200 Ma (Figures 6a and 6b), the restorations of Siberia were located at lower latitudes and exhibited clearer CW rotations, while NCA showed smaller northward displacement and CCW rotations. After correcting the CW TPW event at 200–150 Ma (Figures 6c and 6d), Siberia displayed smaller southward motions and CW rotations, while NCA experienced larger northward displacement and CCW rotations. Similarly, after the TPW correction at 150–140 Ma (Figures 6e and 6f), Siberia showed smaller southward displacements and CW rotations, while NCA exhibited more northward displacements. It is worth noting that the TPW corrected reconstructions should be interpreted with caution, because the finite rotations of the TPW events [*Torsvik et al*., 2012, Table 12] are estimated under the assumption that the central eastern Eurasian plates including NCA have moved as a rigid plate with stable Europe during the Mesozoic. In view that many high-quality Asian paleopoles have been recently acquired, future work could apply the APWPGP method to evaluate the APM history of the Chinese and Southeast Asian plates, which cannot be constrained by transferring rotations through plate circuits.

To investigate the time-varying kinematics of the Siberian and NCA sides of the suture zone during the closing of the MOO, we compute the time-dependent velocity vectors in 10 Myr intervals of three reference points on the suture (see Figure 5a), relative to both the present-day spin axis (Figures 7a and 7b) and the mantle (Figures 7c and 7d). We then calculate the convergence rates of the suture boundaries in the coordinates of the three reference points that, regardless of the TPW corrections, reveal three stages during the closing of the MOO between 260 Ma and 120 Ma. As discussed earlier, potential TPW events do not change our kinematic reconstructions of the closing of the MOO, because variations in the positions of the spin axis were relative to both Siberia and NCA. However, reconstructions of Siberia and NCA are significantly different with and without the TPW corrections.

Compared with previous studies, where paleolongitudes of Siberia are speculated using additional tie points to long-lasting mantle structures [*Kuzmin et al*., 2010; *Torsvik et al*., 2010] and/or sinking slabs [*van der Meer et al*., 2010; *Van der Voo et al*., 2015], in this work we use paleomagnetic data to independently constrain its APM history during the last 260 Myr. We also independently derive the finite rotations for NCA that cannot be predicted by transferring rotations using plate circuits. Reconstruction discrepancies arise due to different approaches to constraining paleolongitudes. For example, *Kuzmin et al*. [2010] reconstruct Siberia at 250 Ma to the present-day location of either Iceland or eastern stable Europe, beneath which there are arguably long-lasting chemical/thermal structures near the core-mantle boundary [*Torsvik et al*., 2008]. *Smirnov and Tarduno* [2010] adopt a circle fit (similar to our approach) to their compiled Siberian paleopoles and reconstruct Siberia at 250 Ma to the present-day location of northwestern stable Europe. Their restored Siberia is located in similar paleolongitudes but lower paleolatitudes compared to our reconstruction, because we apply the paleolatitude correction described in *Wu and Kravchinsky* [2014]. Larger discrepancies are expected between different reconstructions of NCA because (1) it had a separate motion history before its amalgamation with Eurasia and (2) lack of strict paleolongitude constraints in previous studies. One notable discrepancy is that our TPW-corrected reconstructions of NCA at 250–200 Ma are ~20–25° farther east of those estimated based on slab identification using a *P* velocity model [*van der Meer et al*., 2010; *Van der Voo et al*., 2015]. Significant

discrepancy could arise in the predicted slab location and morphology using different tomography models (see detailed discussion in section 6.3).

The final closure of the MOO remnant basin might have been accomplished at 130–120 Ma, as seen from the overlapping Siberian and NCA suture margins at 120 Ma (Figures 6e and 6f). This is supported by the small convergence rate of Siberia and NCA ~0.4–0.6 cm/yr at the time (Figure 7). The deduced closure timing is consistent with the underlying slab distribution: the slabs (subducted at 140–120 Ma) associated with the MOO lithosphere display a southward migration relative to the restored suture margins at the depths of 1700–1325 km (Figure 9), indicating a relocation of subduction zones away from the suture zone in the last stage of suturing (see detailed discussion in section 6.2). Intriguingly, the continuous convergence between Siberia and NCA until 120 Ma provides a kinematic explanation for the resolved fast velocity anomalies (i.e., slabs) at the depth of 1325 km from GAP-P4 and MIT-P near the restored suture margins (they are not seen the *S* velocity models). In comparison, *Van der Voo et al*. [2015] propose ~160–140 Ma for the final closure of the MOO remnant basin. This older age estimate is derived from (1) the reconstructions of Siberia and NCA based on the location and orientation of the MOO slab predicted from their adopted *P* velocity model and (2) the statistically indistinguishable paleolatitudes of the suture margins since 150 Ma (Figure 5d) [*Van der Voo et al*., 2015]. Note that no NCA paleopole at 140 Ma is available now and additional work of obtaining high-quality data is the key to resolving the dispute on the final closure age. Future seismological and geodynamic studies are also needed to confirm that the fast-velocity anomalies near the restored suture margins resolved from GAP-P4 and MIT-P are related to the subduction of the MOO lithosphere.

We observe anomalous reconstructions between Siberia and NCA at 60 Ma (overlap), 70 Ma (gap), and 110 Ma (overlap) (Figures 6g and 6h). These anomalies could partly result from the fact that both the North China and Siberian (stable European) APWPs are constructed with a common shallowing factor of 0.6 [*Torsvik et al*., 2012; *Van der Voo et al*., 2015]. These reconstructions are anomalous compared to those at 100–80 Ma, when the restored suture boundaries fit well. In traditional paleomagnetic reconstructions, such postsuturing anomalous reconstructions are commonly reconciled within errors because geological observations do not support continental shortening or divergence at these ages. We illustrate here the prereconciled reconstructions so readers have a complete understanding and assessment of the APWPGP method. Note that imperfect postsuturing paleopoles will not affect the robustness of the presuturing reconstructions, because stage rotations are derived from the trends (i.e., geometries) of the identified APWP tracks rather than individual paleopoles. To a large extent, these prereconciled anomalous reconstructions demonstrate that reconstructions from the APWPGP method are closer to the paleomagnetic data [see *Van der Voo et al*., 2015, Figure 4] compared to other APM methods. For future application of our reconstructions, readers can either adjust the finite rotations of the NCA at 60 Ma, 70 Ma and 110 Ma within errors based on additional observations or simply adopt the coeval finite rotations of Siberia (stable Europe).

6. Discussion

6.1. TPW Corrections Before or After Circle Fits?

An APWP results from a combination of APMs and TPW episodes (i.e., APWP = APM · TPW), and theoretically removing TPW effects from the APWP either before or after circle fits should not change the resulting APMs relative to the mantle. However, it is possible that TPW-corrected APWPs may lead to different circle fits and associated reconstructions in the mantle frame. One may therefore wonder how the reconstructed closing of the MOO with respect to the mantle are affected if circle fits are applied to the TPW-corrected Siberian and North China APWPs (Table S7).

We identify the same APWP tracks at the same intervals (Figure S2), to which both the GC and SC methods are applied to derive stage rotations. The GC fits are adopted to calculate the finite reconstruction parameters based on a statistical comparison of the GC and SC fits (Tables S8 and S9). The resulting APMs in the mantle frame are illustrated in Figures S3 and S4.

Compared to those derived by removing the TPW effects from reconstructions (Figure 6), the APMs of Siberia and NCA from their TPW-corrected APWPs show less motion distances (Figures S3 and S4a): the restorations of Siberia exhibit less pre-100 Ma motion distances, and those of NCA display less pre-200 Ma motion distances. The discrepancies are clearly illustrated by the variations in the great circle distances (GCDs)

between the reconstructions that are calculated by applying TPW corrections both before and after circle fits (Figure S4b): there are significant increases in the GCDs at the intervals of 120–100 Ma for Siberia and of 210–190 Ma for NCA, respectively. The same three stages between 260 Ma and 120 Ma are disclosed during the closing of the MOO from the APMs derived from the TPW-corrected APWPs (Figure S4c). However, compared to those associated with the reconstructions corrected for the TPW effects after circle fits (Figure 7), the resulting GCDs are smaller in the older two stages but larger in the youngest stage at 150–120 Ma (Figure S4c). As a result of the different GCDs, the APMs of Siberia and NCA derived from the TPW-corrected APWPs also exhibit smaller convergence rates at the interval of 200–150 Ma but larger ones at the interval of 150–120 Ma (Figures S4c and 7). The anomalously large GCDs at the interval of 150–120 Ma could be reconcilable after including errors in the TPW effects (errors in the TPW estimates are not propagated here because they are not provided by their authors). We therefore recommend applying TPW corrections after circle fits, both to reduce the dependence of our results on the robustness of the former TPW estimates and to avoid anomalous reconstructions due to improper error propagations associated with the TPW corrections.

The reader should be aware that it is a common practice to assume that both plate motions and TPW effects are piecewise constant at given time intervals for simplicity. In reality, this may not be the case. For example, the Cretaceous period is divided into early and late epochs with durations of circa 40 and 35 Myr, respectively. Uncertainties associated with the age translation for the North China paleopoles could result in errors in the restored plate motions, because very few paleopoles in the Cretaceous are dated to a better precision than the epoch level [*Van der Voo et al*., 2015]. Another example is that the former TPW episodes are approximated with constant speeds [*Steinberger and Torsvik*, 2008; *Torsvik et al*., 2012]. However, given the dynamics of TPW, it is mostly likely that episodes of TPW start slow become faster and then slower again [*Steinberger and Torsvik*, 2010].

6.2. Closing of the MOO and Slab Morphology Beneath Eurasia

The time-dependent convergence rates of the suture boundaries more clearly reveal three stages during the closing of the MOO between 250 Ma and 120 Ma, i.e., 250–200 Ma, 200–150 Ma, and 150–120 Ma (Figure 7). These stages divide the lower mantle into three depth intervals according to the time scales of *van der Meer et al*. [2010]: 2800–2392 km, 2300–1819 km, and 1819–1325 km. We investigate how past plate motions are related to the distribution and production of the MOO slabs from their areas associated with intraoceanic and continental-oceanic subduction (Figures 9–11, see section 3.4 for the detailed methods).

The first stage featured the subduction of approximately 62.5–76.1% of the MOO lithosphere between Siberia and NCA at 260–200 Ma, as estimated from the sum of percentage slab areas inside the polygons of the TPW-corrected restorations of Siberia and NCA and of the MOO basin at the depths of 2300–2800 km (first row in Figure 9). For example, the value 76.1% is calculated from the sum of the areas of slabs related to intraoceanic subduction (57.8%) and continental-oceanic subduction (18.3%) using the *P* velocity model GAP-P4 (first row in Figure 9a). Consistent with the massive subduction, spherical distance between the two suture edges was reduced by ~66.7% at a convergence rate of ~8.8 ± 0.6 cm/yr at the interval (Figure 7). This massive subduction was conducted primarily through an intraoceanic convergence (40.7–57.8%) on paleotrenches that were located in middle eastern Eurasia, along with approximately 18.3–21.8% continental-oceanic convergence in the vicinity of reconstructed Siberia and NCA (first row in Figure 9 and Figure 10). The amount of slab formation through intraoceanic subduction in the stage decreased at a near-constant rate according to both the *S* velocity and *P* velocity models (Figure 11), indicating a persistent subduction speed along the paleotrenches.

The second stage at 200–150 Ma saw the subduction of approximately 14.2–30.6% of the total MOO lithosphere, predominantly in the vicinity of NCA and southwest of Siberia (middle row in Figure 9 and Figure 11). During this stage, subduction appeared to be concentrated in a zone stretching from southwestern Siberia through eastern China to the northwestern Pacific. Despite discrepancies in the prediction of detailed slab features, various tomography models are consistent in revealing long-wavelength features such as the slabs surrounding the reconstructed NCA at 180 Ma (middle row in Figure 9 and Figure 10). During this stage, spherical distance between the suture edges was reduced by another 21.1% with a slower average convergence rate of ~3.6 ± 0.3 cm/yr (Figure 7). Subduction at the interval also occurred at a much slower speed, as seen from the gently left inclined trend of slab areas at the depth of 2300–1800 km (Figure 11).

Slab production through continental-oceanic subduction outpaced that through intraoceanic subduction at the two younger intervals (Figure 11). According to the tomographic models, such outpacing should have occurred no later than 150 Ma when areas of slabs resulting from the two different mechanisms are statistically distinguishable (Figure 11).

Based on the insignificant convergence rates (~0.4–0.6 cm/yr) (Figure 7), the interval of 150–120 Ma was the last stage in closing the remnant paleooceanic basin between Siberia and NCA. This is supported by the opposite senses of rotations of the two continents (Figures 6e, 6f, and 7) and strongly overlapping paleopoles (Figure 3) and reconstructions (Figure 5a). Consistent with our APM reconstructions, all the adopted tomographic models resolve a southward migration of slabs at the depth of 1819–1325 km (i.e., ancient subduction zones) relative to the restored MOO suture margins (bottom row in Figure 9). The *P* velocity models GAP-P4 and MIT-P also predict fast velocity anomalies near the suture boundaries at 120 Ma inside reconstructed Siberia and NCA, indicating the final stage of the subduction of the MOO (bottom row in Figures 9a and 9b). In comparison, the predicted fast-velocity anomalies from the *S* velocity model S40RTS are not immediately close to the suture margins, and no similar fast-velocity anomalies are seen from the *S* velocity mean model s10mean.

To investigate the relationships between convergence rates and slab areas, we calculate the Pearson correlation coefficients between the GCDs between the reconstructed suture margins and areas of slabs related to intraoceanic and continental-oceanic subduction from different tomographic models (Figure S5). This analysis is based on the age-depth relationship for the lower mantle [*van der Meer et al*., 2010]. A robust linear relationship is revealed between the GCDs and area of slabs associated with intraoceanic subduction, for which the correlation coefficients are larger than 0.95 from the tomographic models (Figure S5). The linear relationship between the GCDs and slab area is slightly improved when the contribution from continental-oceanic subduction is included. However, no clear linear relationships are revealed between the GCDs and the area of slabs related to continental-oceanic subduction. This indicates that reduced GCDs had been predominantly accommodated by intraoceanic subduction whose rates are strongly related to convergence rates (i.e., reduction rates in the GCDs).

Note that it is difficult to distinguish between different origins of slabs if subduction was located close to a continent-ocean boundary. In this situation, a small portion of slabs enclosed in the reconstructed MOO basin polygons were, in fact, formed by continental-oceanic subduction. In addition, subduction of the Tethys and Panthalassa could induce uncertainties in our estimated MOO slab areas enclosed in the reconstructions (they are likely the result of continental-oceanic subduction). Unfortunately, it is still a challenge to identify the origins of slabs simply based on plate reconstructions and tomographic models. Future advances in describing the time-dependent variations in subduction zone properties in the region (e.g., subduction zone dip angles) will provide insights into the issue. However, such difficulty does not affect our conclusions that the majority of the MOO slabs in the region were formed at 250–150 Ma when the spherical distance between the reconstructed suture margins was reduced by approximately 87.8% and that slabs formed at later ages were primarily the result of continental-oceanic subduction.

6.3. Slab Characterization From Various Tomography Models

The adopted global tomography models are overall consistent in revealing long-wavelength (>1000 km) fast-velocity structures, such as the slab graveyard in the lowermost mantle beneath middle East Eurasia (top row in Figure 9 and Figure 10). Predictions of slab distribution from these models also show consistency with our kinematic reconstructions, as reflected from the robust spatial correlation between the past plate motions and the present-day descending mantle features associated with the closing of MOO (Figure 9). In addition, all the models predict comparable cumulative percentage consumption of the total MOO lithosphere at the three depth intervals corresponding to the stages defined by our reconstructions (see values in Figure 9).

However, different tomography models are quite distinct in predicting geometry and/or area of intermediate-wavelength (500–1000 km) fast-velocity anomalies in the lower mantle (Figures 9–11). One example is that s10mean predicts a continuous and more smoothed slab zone extending from the Norwegian Sea to the western Pacific Ocean at the depths below 2500 km (top row in Figure 9), which likely results from the fact that s10mean is constructed by averaging a variety of *S* velocity models [*Doubrovine*

et al., 2016]. In comparison, such smooth fast-velocity anomalies are not seen from the rest of the models (Figures 9 and 10). Another example is that some fast velocity features such as those inside the restored locations of Siberia and NCA at 120 Ma display various shapes and locations according to different tomographic models (bottom row in Figure 9). These fast-velocity anomalies, if confirmed to be slabs, would represent subduction along the central segment of the suture at the final stage of closing of the MOO (bottom row in Figures 9a and 9b). Future regional seismological and geodynamic studies are needed to explain the origin of these velocity anomalies. However, these intermodel discrepancies will not affect the robustness of our first-order correlation between past plate kinematics and slab distribution.

The intermodel discrepancies discussed above can be partly attributed to different selections of reference velocity model. Specifically, percentage velocity perturbations from MIT-P and S40RTS are relative to the preliminary reference Earth model [*Dziewonski and Anderson*, 1981], while those from GAP-P4 and s10mean are relative to the reference velocity model IASP91 [*Kennett and Engdahl*, 1991] and layer-dependent means from each of the input models [*Doubrovine et al*., 2016], respectively. In addition, earlier studies have shown a reduced correlation between the shear and compressional wave speeds [*Ishii and Tromp*, 1999; *Masters et al*., 2000; *Trampert et al*., 2004] along with an anticorrelation between the shear wave speed and bulk sound speed below 2500 km [*Simmons et al*., 2010]. Below ~2600 km, the phase transition layer "*D*" where perovskite is converted to postperovskite could cause an ~2% increase in *S* velocity and a small decrease or increase in *P* velocity [*Garnero and McNamara*, 2008]. A recent study of mantle dynamics suggests that strong silica-enriched domains can significantly affect mantle convection pattern and cause variations in the morphology of the fast velocities in the lower mantle [*Ballmer et al*., 2017]. Such compositional heterogeneity might induce uncertainties in the area of slabs estimated from the adopted tomographic models. Other reasons for the intermodel discrepancies include inversions using different waveform data sets, parameterizations, and regularization schemes [*Lekic et al*., 2012].

Note that the reported spatial-temporal correlation between our APM reconstructions and slab distribution is based on the time scales that are constructed under the assumption of vertical slab sinking [*van der Meer et al*., 2010]. Nonvertical slab sinking would affect the validity of the time scales and cause uncertainties in the interpreted subduction scenarios in the context of our kinematic reconstructions. The issue is further complicated by the fact that existing time scales of slab sinking are commonly determined from one selection of many global tomography models [*van der Meer et al*., 2010; *Butterworth et al*., 2014], among which large intermodel discrepancies exist in slab predictions. Further geodynamic studies of mantle flow requiring kinematic reconstructions as input surface conditions are needed to provide insights to the issue. To this end, our reconstructed Siberia and NCA along with the global APM model in the coordinates of stable Europe (Table 1) should be incorporated in modeling the time-dependent mantle circulation.

7. Conclusions

In this study, we adopt a novel absolute plate motion reconstruction method to independently restore the plate motions of Siberia and North China-Amuria (NCA), which had bounded the Mongol-Okhotsk Ocean (MOO) during the Mesozoic. Our reconstructions shed light on how slabs related to the subduction of the MOO affect the geometry of fast-velocity anomalies in the lower mantle. Three stages, i.e., 250–200 Ma, 200–150 Ma and 150–120 Ma, are identified from the time-varying convergence rates of Siberia and NCA. The first two stages witnessed a reduction of approximately 87.8% of the spherical distance between Siberia and NCA, with a decrease in their convergence rate from 8.8 ± 0.6 cm/yr to 3.6 ± 0.3 cm/yr. More than 90% of the slabs associated with the MOO were formed during the two stages mainly through intraoceanic convergence and then ocean-continent subduction. The last stage of closing the remnant MOO basin was 150–120 Ma when approximately 4.6–9.8% slabs associated with the MOO lithosphere were formed and the convergence rate of the suture margins was reduced to 0.4–0.6 cm/yr.

Acknowledgments
The data used are listed in the references, tables, and supporting information. Calculation and visualization of the absolute plate motion reconstructions were performed with the freeware PMTec and GPlates. We thank Claire Currie, Aleksey Smirnov, Douwe van Hinsbergen, and three anonymous reviewers for their invaluable comments that greatly improved an earlier version of this manuscript. We thank Pavel Doubrovine for sharing his tomographic model s10mean. We thank Wim Spakman for the helpful suggestions on selecting tomographic models. The project was funded by the 973 research grant 2015CB452602 and the Natural Sciences and Engineering Research Council of Canada grants RGPIN-2014-04183, RES0029444, and 386245/2010.

References

Anderson, D. L., and A. M. Dziewonski (1984), Seismic tomography, *Sci. Am.*, *251*(4), 60–68.

Ballmer, M. D., C. Houser, J. W. Hernlund, R. M. Wentzcovitch, and K. Hirose (2017), Persistence of strong silica-enriched domains in the Earth's lower mantle, *Nat. Geosci.*, *10*, 236–240.

Besse, J., and V. Courtillot (2002), Apparent and true polar wander and the geometry of the geomagnetic field over the last 200 Myr, *J. Geophys. Res.*, *107*(B11), 2300, doi:10.1029/2000JB000050.

Burke, K., and T. H. Torsvik (2004), Derivation of large igneous provinces of the past 200 million years from long-term heterogeneities in the deep mantle, *Earth Planet. Sci. Lett.*, *227*(3), 531–538.
Butterworth, N., A. Talsma, R. Müller, M. Seton, H.-P. Bunge, B. Schuberth, G. Shephard, and C. Heine (2014), Geological, tomographic, kinematic and geodynamic constraints on the dynamics of sinking slabs, *J. Geodyn.*, *73*, 1–13.
Chen, Z., L. Zhang, B. Wan, H. Wu, and N. Cleven (2011), Geochronology and geochemistry of the Wunugetushan porphyry Cu–Mo deposit in NE China, and their geological significance, *Ore Geol. Rev.*, *43*(1), 92–105.
Cocks, L. R. M., and T. H. Torsvik (2007), Siberia, the wandering northern terrane, and its changing geography through the Palaeozoic, *Earth Sci. Rev.*, *82*(1–2), 29–74.
Cogné, J.-P., J. Besse, Y. Chen, and F. Hankard (2013), A new Late Cretaceous to present APWP for Asia and its implications for paleomagnetic shallow inclinations in central Asia and Cenozoic Eurasian plate deformation, *Geophys. J. Int.*, *192*(3), 1000–1024.
Courtillot, V. (2007), True polar wander, in *Encyclopedia of Geomagnetism and Paleomagnetism*, pp. 956–969, Springer, Dordrecht, Netherlands.
Cox, A., and R. B. Hart (1986), *Plate Tectonics: How It Works*, pp. 219–254, Blackwell Sci. Publ., Malden, Mass.
Donskaya, T., D. Gladkochub, A. Mazukabzov, and A. Ivanov (2013), Late Paleozoic–Mesozoic subduction-related magmatism at the southern margin of the Siberian continent and the 150 million-year history of the Mongol-Okhotsk Ocean, *J. Asian Earth Sci.*, *62*, 79–97.
Doubrovine, P. V., B. Steinberger, and T. H. Torsvik (2012), Absolute plate motions in a reference frame defined by moving hot spots in the Pacific, Atlantic, and Indian oceans, *J. Geophys. Res.*, *117*, B09101, doi:10.1029/2011JB009072.
Doubrovine, P. V., B. Steinberger, and T. H. Torsvik (2016), A failure to reject: Testing the correlation between large igneous provinces and deep mantle structures with EDF statistics, *Geochem. Geophys. Geosyst.*, *17*, 1130–1163, doi:10.1002/2015GC006044.
Dziewonski, A. M., and D. L. Anderson (1981), Preliminary reference Earth model, *Phys. Earth Planet. Inter.*, *25*(4), 297–356.
Embleton, B. J., M. W. McElhinny, X. Ma, Z. Zhang, and Z. X. Li (1996), Permo-Triassic magnetostratigraphy in China: The type section near Taiyuan, Shanxi province, North China, *Geophys. J. Int.*, *126*(2), 382–388.
Enkin, R. J., Z. Yang, Y. Chen, and V. Courtillot (1992), Paleomagnetic constraints on the geodynamic history of the major blocks of China from the Permian to the present, *J. Geophys. Res.*, *97*, 13,953–13,989, doi:10.1029/92JB00648.
Fisher, N. I., T. Lewis, and B. J. Embleton (1987), *Statistical Analysis of Spherical Data*, pp. 140–144, Cambridge Univ. Press, Cambridge.
Fritzell, E., A. Bull, and G. Shephard (2016), Closure of the Mongol–Okhotsk Ocean: Insights from seismic tomography and numerical modelling, *Earth Planet. Sci. Lett.*, *445*, 1–12.
Garnero, E. J., and A. K. McNamara (2008), Structure and dynamics of Earth's lower mantle, *Science*, *320*(5876), 626–628.
Gradstein, F. M., J. G. Ogg, and M. Schmitz (2012), *The Geologic Time Scale 2012*, vol. 2, 1144 pp., Elsevier, Amsterdam.
Gray, N. H., P. A. Geiser, and J. R. Geiser (1980), On the least-squares fit of small and great circles to spherically projected orientation data, *J. Int. Assoc. Math. Geol.*, *12*(3), 173–184.
Hager, B. H., R. W. Clayton, M. A. Richards, R. P. Comer, and A. M. Dziewonski (1985), Lower mantle heterogeneity, dynamic topography and the geoid, *Nature*, *313*(6003), 541–545.
Huang, B., R. Shi, Y. Wang, and R. Zhu (2005), Palaeomagnetic investigation on Early–Middle Triassic sediments of the North China Block: A new Early Triassic palaeopole and its tectonic implications, *Geophys. J. Int.*, *160*(1), 101–113.
Ishii, M., and J. Tromp (1999), Normal-mode and free-air gravity constraints on lateral variations in velocity and density of Earth's mantle, *Science*, *285*(5431), 1231–1236.
Kennett, B., and E. Engdahl (1991), Traveltimes for global earthquake location and phase identification, *Geophys. J. Int.*, *105*(2), 429–465.
Khramov, A. N. (1987), *Paleomagnetology*, Springer, Berlin.
Kravchinsky, V. A., J.-P. Cogné, W. P. Harbert, and M. I. Kuzmin (2002a), Evolution of the Mongol–Okhotsk Ocean as constrained by new palaeomagnetic data from the Mongol–Okhotsk suture zone, Siberia, *Geophys. J. Int.*, *148*(1), 34–57.
Kravchinsky, V. A., A. A. Sorokin, and V. Courtillot (2002b), Paleomagnetism of Paleozoic and Mesozoic sediments from the southern margin of Mongol-Okhotsk Ocean, far eastern Russia, *J. Geophys. Res.*, *107*(B10), 2253, doi:10.1029/2001JB000672.
Kurihara, T., et al. (2009), Upper Silurian and Devonian pelagic deep-water radiolarian chert from the Khangai–Khentei belt of central Mongolia: Evidence for Middle Paleozoic subduction–accretion activity in the central Asian orogenic belt, *J. Asian Earth Sci.*, *34*(2), 209–225.
Kuzmin, M. I., V. V. Yarmolyuk, and V. A. Kravchinsky (2010), Phanerozoic hot spot traces and paleogeographic reconstructions of the Siberian continent based on interaction with the African large low shear velocity province, *Earth Sci. Rev.*, *102*(1), 29–59.
Lay, T., J. Hernlund, and B. A. Buffett (2008), Core–mantle boundary heat flow, *Nat. Geosci.*, *1*(1), 25–32.
Lekic, V., S. Cottaar, A. Dziewonski, and B. Romanowicz (2012), Cluster analysis of global lower mantle tomography: A new class of structure and implications for chemical heterogeneity, *Earth Planet. Sci. Lett.*, *357*, 68–77.
Li, C., R. D. van der Hilst, E. R. Engdahl, and S. Burdick (2008), A new global model for P wave speed variations in Earth's mantle, *Geochem. Geophys. Geosyst.*, *9*, Q05018, doi:10.1029/2007GC001806.
Lithgow-Bertelloni, C., and P. G. Silver (1998), Dynamic topography, plate driving forces and the African superswell, *Nature*, *395*(6699), 269–272.
Ma, X., L. Xing, Z. Yang, S. Xu, and J. Zhang (1993), Palaeomagnetic study since Late Paleozoic in the Ordos Basin, *Chin. J. Geophys.*, *36*(1), 68–79.
Masters, G., G. Laske, H. Bolton, and A. Dziewonski (2000), The relative behavior of shear velocity, bulk sound speed, and compressional velocity in the mantle: Implications for chemical and thermal structure, *Earth's Deep Interior: Mineral Physics and Tomography from the Atomic to the Global Scale*, pp. 63–87, AGU, Washington, D. C.
McElhinny, M., B. Embleton, X. Ma, and Z. Zhang (1981), Fragmentation of Asia in the Permian, *Nature*, *293*, 212–216.
Meng, Z., R. Coe, and G. Frost (1989), Paleomagnetic results from Late Permian Redbeds in Gansu Province, China, *Eos Trans. AGU*, *70*, 1070.
Metelkin, D. V., V. A. Vernikovsky, A. Y. Kazansky, and M. T. Wingate (2010), Late Mesozoic tectonics of central Asia based on paleomagnetic evidence, *Gondwana Res.*, *18*(2), 400–419.
Mitchell, R. N., T. M. Kilian, and D. A. Evans (2012), Supercontinent cycles and the calculation of absolute palaeolongitude in deep time, *Nature*, *482*(7384), 208–211.
Morgan, W. J. (1971), Convection plumes in the lower mantle, *Nature*, *230*, 42–43.
Müller, R. D., J.-Y. Royer, and L. A. Lawver (1993), Revised plate motions relative to the hotspots from combined Atlantic and Indian Ocean hotspot tracks, *Geology*, *21*(3), 275–278.
Obayashi, M., J. Yoshimitsu, G. Nolet, Y. Fukao, H. Shiobara, H. Sugioka, H. Miyamachi, and Y. Gao (2013), Finite frequency whole mantle *P* wave tomography: Improvement of subducted slab images, *Geophys. Res. Lett.*, *40*, 5652–5657, doi:10.1002/2013GL057401.
Panet, I., G. Pajot-Métivier, M. Greff-Lefftz, L. Métivier, M. Diament, and M. Mandea (2014), Mapping the mass distribution of Earth's mantle using satellite-derived gravity gradients, *Nat. Geosci.*, *7*(2), 131–135.

Raub, T., J. Kirschvink, and D. Evans (2007), True polar wander: Linking deep and shallow geodynamics to hydro-and biospheric hypotheses, *Treatise Geophys.*, *5*, 565–589.

Ren, Q., S. Zhang, H. Wu, Z. Liang, X. Miao, H. Zhao, H. Li, T. Yang, J. Pei, and G. A. Davis (2016), Further paleomagnetic results from the ~155 Ma Tiaojishan Formation, Yanshan Belt, North China, and their implications for the tectonic evolution of the Mongol–Okhotsk suture, *Gondwana Res.*, *35*, 180–191.

Richards, M. A., and B. H. Hager (1984), Geoid anomalies in a dynamic Earth, *J. Geophys. Res.*, *89*, 5987–6002, doi:10.1029/JB089iB07p05987.

Ritsema, J., A. Deuss, H. van Heijst, and J. Woodhouse (2011), S40RTS: A degree-40 shear-velocity model for the mantle from new Rayleigh wave dispersion, teleseismic traveltime and normal-mode splitting function measurements, *Geophys. J. Int.*, *184*(3), 1223–1236.

Shephard, G. E., H.-P. Bunge, B. S. Schuberth, R. Müller, A. Talsma, C. Moder, and T. Landgrebe (2012), Testing absolute plate reference frames and the implications for the generation of geodynamic mantle heterogeneity structure, *Earth Planet. Sci. Lett.*, *317*, 204–217.

Shi, R., B. Huang, R. Zhu, and S. Ren (2004), Paleomagnetic study on the Early Triassic red beds from Jiaocheng, Shanxi Province, *Sci. China Ser. D Earth Sci.*, *47*(2), 108–114.

Simmons, N. A., A. M. Forte, L. Boschi, and S. P. Grand (2010), GyPSuM: A joint tomographic model of mantle density and seismic wave speeds, *J. Geophys. Res.*, *115*, B12310, doi:10.1029/2010JB007631.

Simmons, N., S. Myers, G. Johannesson, E. Matzel, and S. Grand (2015), Evidence for long-lived subduction of an ancient tectonic plate beneath the southern Indian Ocean, *Geophys. Res. Lett.*, *42*, 9270–9278, doi:10.1002/2015GL066237.

Smirnov, A. V., and J. A. Tarduno (2010), Co-location of eruption sites of the Siberian traps and North Atlantic Igneous Province: Implications for the nature of hotspots and mantle plumes, *Earth Planet. Sci. Lett.*, *297*(3), 687–690.

Steinberger, B., and T. H. Torsvik (2008), Absolute plate motions and true polar wander in the absence of hotspot tracks, *Nature*, *452*(7187), 620–623.

Steinberger, B., and T. Torsvik (2010), Toward an explanation for the present and past locations of the poles, *Geochem. Geophys. Geosyst.*, *11*, Q06W06, doi:10.1029/2009GC002889.

Tan, X., D. Fang, Y. Yuan, S. Fan, and J. Bao (1991), Paleomagnetic study on red beds, Liujiaogou Formation (TRL) from Taoyuan, Yaoqu, Jixian, Shanxi Province, *Acta Geophys. Sin.*, *34*(6), 736–743.

Tarduno, J. A., and J. Gee (1995), Large-scale motion between Pacific and Atlantic hotspots, *Nature*, *378*(6556), 477–480.

Tomurtogoo, O., B. Windley, A. Kröner, G. Badarch, and D. Liu (2005), Zircon age and occurrence of the Adaatsag ophiolite and Muron shear zone, central Mongolia: Constraints on the evolution of the Mongol–Okhotsk Ocean, suture and orogen, *J. Geol. Soc.*, *162*(1), 125–134.

Torsvik, T. H., R. D. Müller, R. Van der Voo, B. Steinberger, and C. Gaina (2008), Global plate motion frames: Toward a unified model, *Rev. Geophys.*, *46*, RG3004, doi:10.1029/2007RG000227.

Torsvik, T. H., K. Burke, B. Steinberger, S. J. Webb, and L. D. Ashwal (2010), Diamonds sampled by plumes from the core-mantle boundary, *Nature*, *466*(7304), 352–355.

Torsvik, T. H., et al. (2012), Phanerozoic polar wander, palaeogeography and dynamics, *Earth Sci. Rev.*, *114*(3–4), 325–368.

Trampert, J., F. Deschamps, J. Resovsky, and D. Yuen (2004), Probabilistic tomography maps chemical heterogeneities throughout the lower mantle, *Science*, *306*(5697), 853–856.

van der Hilst, R. D., and H. Kárason (1999), Compositional heterogeneity in the bottom 1000 kilometers of Earth's mantle: Toward a hybrid convection model, *Science*, *283*(5409), 1885–1888.

van der Meer, D. G., W. Spakman, D. J. van Hinsbergen, M. L. Amaru, and T. H. Torsvik (2010), Towards absolute plate motions constrained by lower-mantle slab remnants, *Nat. Geosci.*, *3*(1), 36–40.

Van der Voo, R. (1990), Phanerozoic paleomagnetic poles from Europe and North America and comparisons with continental reconstructions, *Rev. Geophys.*, *28*, 167–206, doi:10.1029/RG028i002p00167.

Van der Voo, R., W. Spakman, and H. Bijwaard (1999), Mesozoic subducted slabs under Siberia, *Nature*, *397*(6716), 246–249.

Van der Voo, R., D. J. J. van Hinsbergen, M. Domeier, W. Spakman, and T. H. Torsvik (2015), Latest Jurassic–earliest Cretaceous closure of the Mongol-Okhotsk Ocean: A paleomagnetic and seismological-tomographic analysis, in *Late Jurassic Margin of Laurasia—A Record of Faulting Accommodating Plate Rotation, Geol. Soc. Am. Spec. Pap.*, *513*, edited by T. H. Anderson et al., pp. 1–18, doi:10.1130/2015.2513(19).

Williams, S., N. Flament, R. D. Müller, and N. Butterworth (2015), Absolute plate motions since 130 Ma constrained by subduction zone kinematics, *Earth Planet. Sci. Lett.*, *418*, 66–77.

Wu, L., and V. A. Kravchinsky (2014), Derivation of paleolongitude from the geometric parametrization of apparent polar wander path: Implication for absolute plate motion reconstruction, *Geophys. Res. Lett.*, *41*, 4503–4511, doi:10.1002/2014GL060080.

Wu, L., V. A. Kravchinsky, and D. K. Potter (2015), PMTec: A new MATLAB toolbox for absolute plate motion reconstructions from paleomagnetism, *Comput. Geosci.*, *82*, 139–151.

Yang, Z., X. Ma, J. Besse, V. Courtillot, L. Xing, S. Xu, and J. Zhang (1991), Paleomagnetic results from Triassic sections in the Ordos Basin, North China, *Earth Planet. Sci. Lett.*, *104*(2–4), 258–277.

Zhao, X., and R. S. Coe (1989), Tectonic implications of perm-Triassic paleomagnetic results from north and south China, *Geophys. Monogr. Ser.*, *50*, 267–283.

Zhao, P., Y. Chen, B. Xu, M. Faure, G. Shi, and F. Choulet (2013), Did the Paleo-Asian Ocean between North China Block and Mongolia Block exist during the late Paleozoic? First paleomagnetic evidence from central-eastern Inner Mongolia, China, *J. Geophys. Res. Solid Earth*, *118*, 1873–1894, doi:10.1002/jgrb.50198.

Journal of Geophysical Research: Solid Earth

Supporting Information for

Absolute reconstruction of the closing of the Mongol-Okhotsk Ocean in the Mesozoic elucidates the genesis of the slab geometry underneath Eurasia

Lei Wu[1,2]*, Vadim A. Kravchinsky[1], Yu J. Gu[1] & David K. Potter[1]

[1] Department of Physics, University of Alberta, Edmonton, Alberta, Canada, T6G 2E1.

[2] CAS Key Laboratory of Mineralogy and Metallogeny, Guangzhou Institute of Geochemistry, CAS, Guangzhou, China, 510640.

E-mail: lei.wu@ualberta.ca

Tel: +1-(780)492-5591; Fax: +1-(780)492-0714

Contents of this file

Text S1

Tables S1-S10

Figures S1-S5

Introduction

The supporting information contains ten tables, five figures and a text summarizing the methods of apparent polar wander paths geometric parameterizations.

S1. Methods: Apparent polar wander paths geometric parameterizations

The following methods are formulated by Wu and Kravchinsky [2014] and are implemented by the freeware PMTec [Wu et al., 2015].

S1.1. Circle parametrizations

To parametrize apparent polar wander path (APWP) segments for rotation parameters, Wu and Kravchinsky [2014] apply an iterative algorithm of Fisher et al. [1987], where the optimal circle centers $\widehat{\theta}'(x,y,z)$ (row vectors in the Cartesian coordinate system) are derived by minimizing the sums of squares of their angular distances (ψ_i) from the individual paleopoles $\widehat{\lambda_{\mathbf{i}}}'(l_i,m_i,n_i)$ (direction cosines).

$$(l_i,m_i,n_i)\begin{pmatrix} x \\ y \\ z \end{pmatrix} = \cos\psi_i \tag{S1}$$

To start the iteration, an initial estimate of circle center is defined as Fisherian means $\widehat{\theta}'_0(x_0,y_0,z_0)$ of paleopoles along a given APWP track.

$$x_0 = \frac{\sum_{i=1}^{n} l_i}{R}, \quad y_0 = \frac{\sum_{i=1}^{n} m_i}{R}, \quad z_0 = \frac{\sum_{i=1}^{n} n_i}{R}, \tag{S2}$$

$$R = \sqrt{(\sum_{i=1}^{n} l_i)^2 + \sum_{i=1}^{n} (m_i)^2 + \sum_{i=1}^{n} (n_i)^2} \tag{S3}$$

where R is magnitude of the resultant vector.

Repeat the following calculations until the difference between the last two iterates $(\widehat{\theta}^{(j)}, \psi^{(j)})$ and $(\widehat{\theta}^{(j-1)}, \psi^{(j-1)})$ are smaller than 1×10^{-5} degree.

$$\tan \psi_j = \frac{\sum_{i=1}^{n} \sqrt{[1 - (\lambda_i' \widehat{\theta}_{j-1})]}}{\sum_{i=1}^{n} \lambda_i' \widehat{\theta}_{j-1}}, \qquad \widehat{\theta}_j = \frac{\mathbf{Y}}{\sqrt{\mathbf{Y}'\mathbf{Y}}} \tag{S4}$$

where i is the *i*th paleopole along tracks (1, 2, ..., n) and j is iteration number. And

$$\mathbf{Y} = \cos \psi_j \sum_{i=1}^{n} \lambda_i - \sin \psi_j \sum_{i=1}^{n} \mathbf{X}_i, \qquad \mathbf{X}_i = \frac{(\widehat{\lambda}_i' \widehat{\theta}_{j-1}) \widehat{\lambda}_i - \widehat{\theta}_{j-1}}{\sqrt{1 - (\widehat{\lambda}_i' \widehat{\theta}_{j-1})^2}} \tag{S5}$$

Note that the circle fitting method described above results in small circles. Great circles are obtained in some special cases when angular distances (ψ_i) between the best-fit circle centers and paleopoles are 90°. Compared with small circle fit, great circle fit usually presents a smaller amount of displacement and thusly is a relatively conservative option. Instead of setting (ψ_i) to 90°, we adopt an alternative method to calculate great circle centers using orientation matrix T that can be constructed from paleopoles along APWP tracks:

$$\mathbf{T} = \begin{pmatrix} \sum l_i \cdot l_i & \sum l_i \cdot m_i & \sum l_i \cdot n_i \\ \sum m_i \cdot l_i & \sum m_i \cdot m_i & \sum m_i \cdot n_i \\ \sum n_i \cdot l_i & \sum n_i \cdot m_i & \sum n_i \cdot n_i \end{pmatrix} \tag{S6}$$

Great circle rotation center to an APWP track can be calculated from the eigenvector corresponding to the minimum eigenvalue of the orientation matrix **T**. There is no significant difference in great

circle centers calculated from the two methods. Here we choose to use orientation matrix for great circle modelling throughout this work.

Rotation angles Ω_i subtending the modelled APWP tracks are computed from

$$\Omega_i = cos^{-1} \frac{\cos s - \cos p_1 \cos p_2}{\sin p_1 \sin p_2} \tag{S7}$$

where s, p_1 and p_2 represent angular distance between the starting and ending paleopoles, angular distance between the starting pole and Euler pole, and angular distance between the ending pole and Euler pole. Positive sign is assigned to the counterclockwise rotation backward in time (e.g. from 0 to 40 Ma).

Variance ratio V_r is introduced to help decide the better choice of circle modelling:

$$V_r = (n-3)\frac{r_g - r_s}{r_s} \tag{S8}$$

where r_g and r_s represent the sums of squares of angular residuals for great circle and small circle fits respectively [Gray et al., 1980]. Assuming that r_g and r_s are normally distributed, improvement of small circle over great circle fit can be tested at the 0.05 significance level by comparing V_r with $F_{1,n-3}$ [Gray et al., 1980]. The optimal circle modelling combinations for given APWP tracks are decided from reasonable APM reconstructions, which in practice requires trials and modifications.

S1.2. Paleomagnetism-based stage rotation parameters

Rotation matrix R_i can be constructed from paleomagnetic Euler parameters $(\widehat{\theta}_i, -\Omega_i)$, where negative sign before rotation angle signifies counterclockwise rotation during reconstructions [Cox and Hart, 1986].

$$R_i = \begin{pmatrix} x_i x_i(1-\cos\Omega_i)+\cos\Omega_i & x_i y_i(1-\cos\Omega_i)+z_i\sin\Omega_i & x_i z_i(1-\cos\Omega_i)-y_i\sin\Omega_i \\ y_i x_i(1-\cos\Omega_i)-z_i\sin\Omega_i & y_i y_i(1-\cos\Omega_i)+\cos\Omega_i & y_i z_i(1-\cos\Omega_i)+x_i\sin\Omega_i \\ z_i x_i(1-\cos\Omega_i)+y_i\sin\Omega_i & z_i y_i(1-\cos\Omega_i)-x_i\sin\Omega_i & z_i z_i(1-\cos\Omega_i)+\cos\Omega_i \end{pmatrix} \tag{S9}$$

The reconstructed geographic coordinates of a study point $\widehat{\mathbf{P_J}} = (a_1^j, a_2^j, a_3^j)$ can be calculated using matrix multiplication:

$$\widehat{\mathbf{P_J}}^r = \mathbf{R_i}\widehat{\mathbf{P_J}} \tag{S10}$$

where $\widehat{\mathbf{P_J}}^r$ represents the restored reference point.

It is common that real APWPs consist of more than one segment, so stage Euler poles for older tracks need to be derived by closing younger rotations. This can be achieved by combining rotations using matrix multiplication [Cox and Hart, 1986]:

$$\widehat{\theta}_i^r = \mathbf{R_{i-1}}\mathbf{R_{i-2}}\cdots\mathbf{R_1}\widehat{\theta}_i \tag{S11}$$

S1.3. Paleolatitude correction

Because paleopoles are rarely located perfectly on modelled circle tracks, there will be accumulated errors in reconstructions computed from paleomagnetic Euler poles [Smirnov and Tarduno, 2010], leading to incompatible predictions in paleo-colatitudes with paleomagnetic data. To address the issue, Wu and Kravchinsky [2014] suggest the use of paleo-colatitudes determined from paleomagnetism as the spherical distances between the spin axis and restored paleo-positions of a

reference point. This is based on the common paleomagnetic assumption that it is tectonic plates rather than the spin axis that have moved in the geologic history if there are no true polar wander effects.

S1.4. Error analysis

S1.4.1. Errors in circle parameterizations

Errors in the paleomagnetic Euler parameters $(\widehat{\theta}_i, \Omega_i)$ are estimated using a bootstrap procedure. Firstly, individual paleopoles along the modelled APWP tracks are treated as discrete Fisherian distributions, from which 100 new paleopoles are resampled using their precision parameters. This results in 100 new APWPs $(\widehat{\lambda}^{(1)}, \widehat{\lambda}^{(2)}, ..., \widehat{\lambda}^{(n)})$, which are named bootstrapped APWPs. Wu et al. [2015] apply 100 iterations for bootstrap resampling of paleopoles. Secondly, both great circle and small circle fits are implemented to the same segments along the bootstrapped APWPs to calculate the bootstrapped Euler poles $((\widehat{\theta}_{GC}^{(1)}, \widehat{\theta}_{SC}^{(1)}), (\widehat{\theta}_{GC}^{(2)}, \widehat{\theta}_{SC}^{(2)}), ..., (\widehat{\theta}_{GC}^{(100)}, \widehat{\theta}_{SC}^{(100)}))$ and the associated rotation angles. Lastly, confidence ellipses at 0.05 significance in circle fits are estimated from the covariance matrices of the above bootstrapped data sets.

Assuming that the bootstrapped Euler poles are Fisherian distributed, ($\widehat{X}_i$ - $\bar{\mathrm{X}}$) is a chi-square distribution with 2 degrees of freedom (i.e., latitude and longitude), where $\widehat{X}_i$ is the *i*th bootstrapped Euler poles with the Fisherian mean of $\bar{\mathrm{X}}$. As a result, two-dimensional covariance matrices can be constructed, with the major (minor) semi-axes of the confidence ellipses represented by the maximum (minimum) eigenvectors. Note that Euler poles calculated from the main procedure do not necessarily equal to the Fisherian means of the bootstrapped Euler poles. The two data sets should converge when bootstrap resampling repetitions are infinitely large. In practice, we

consider such discrepancies insignificant when their spherical distances are no larger than 5°. Uncertainties in Euler poles are thusly characterized using covariance matrices of the Fisherian means of bootstrapped Euler poles, from which error ellipses are determined in the form of the primary axes (i.e., semi-major and semi-minor) and the angle from the meridian to the right-hand semi-major axis.

S1.4.2. Errors in reconstructions

Errors in reconstructions are also estimated using the chi-square test at the significance level of 0.05, leading to elliptical uncertainty bounds. Errors in reconstructions accumulate gradually back to earlier times and vary based on different selections of reference site. In practice, the center point of a given plate polygon is used to compute ellipses of mean reconstruction errors for the plate.

Table S1: Absolute plate motion (APM) models in the coordinates of different continents. See the main text for the description of the models: M12 - Mitchell et al. [2012]; M10 - van der Meer et al. [2010]; T12 - Torsvik et al. [2012]; T12 TPW - Torsvik et al. [2012]; M93 - Müller et al. [1993]; D12 - Doubrovine et al. [2012]. The M93 model for North America [Müller et al., 1993] is interpolated into 10 Myr steps to facilitate the comparison with other models. Abbreviations: EU - stable Europe, SAF - South Africa, NAM - North America.

Age	Lat	Long	Angle	Lat	Long	Angle	Lat	Long	Angle	Lat	Long	Angle
(Ma)	(°)	(°)	(°)	(°)	(°)	(°)	(°)	(°)	(°)	(°)	(°)	(°)
	M12 - EU			M10 - SAF			T12 - SAF			T12 TPW - SAF		
0	0	0	0	0	0	0	0	83.9	1.5	0	0	0
10	-40.8	30.9	3.8	46.2	-87.9	-1.9	0	80	3.4	0	80	3.4
20	-24.5	46.1	5.4	45.2	-78.6	-4	0	85.6	5.8	0	85.6	5.8
30	-11.1	65.1	7.3	49.7	-70.2	-6.8	0	90.3	7.1	0	90.3	7.1
40	0.5	59.4	7.7	53.1	-55.3	-9.6	0	99	9.5	0	99	9.5
50	6.1	66.3	10.8	51.1	-60.9	-13.1	0	115.6	14.5	0	115.6	14.5
60	13.7	77.1	11.2	43.8	-45.1	-15.9	0	125.3	17.1	0	125.3	17.1
70	20.8	85.2	10.3	44.9	-43.1	-18.2	0	133.3	18.3	0	133.3	18.3
80	27.1	87	10.2	47.3	-41.6	-21.1	0	139.2	19.4	0	139.2	19.4
90	42.1	76.5	12.2	47.2	-39.8	-23.2	0	145.6	20.6	0	145.6	20.6
100	52.1	60.9	15	44	-36.6	-27.2	0	153.2	23	0	153.2	23
110	57.5	117	17.8	35.1	-37.5	-32.7	0	168.7	31.8	0	162.2	24.5
120	58.8	114	22.3	33.1	-33.6	-36.3	0	171.3	36.4	0	166.6	29
130	57.4	118.8	24.7	31.8	-34.4	-39.7	0	170.9	40.7	0	166.9	33.2
140	61.8	72.6	40.9	30.2	-34.9	-44.5	0	172.1	44.2	0	168.8	36.7
150	62.2	79.3	44.1	33.1	-36.7	-44.1	0	167.2	36.9	0	167.2	36.9
160	58.7	94.3	47.4	33.8	-34.1	-43.7	0	165.9	34.6	0	168.4	38.7
170	67.7	62.6	52.7	33.1	-25.2	-45.3	0	163.9	34.1	0	168.7	42.3
180	66.2	52.4	57	31.5	-25	-45.3	0	168.5	27.9	0	175.1	40.7
190	63	37.6	60.7	33	-29.6	-41.1	0	166.6	21.2	0	176.4	40.2
200				29.3	-36.4	-42.3	0	152.2	21	0	171	40.9
210				24	-42.3	-43.7	0	146.3	25.4	0	163	40.1
220	53.5	58.3	64.7	20.3	-46.9	-46.1	0	140.4	31.6	0	153.2	41.4
230	53	68.4	59.3	18.3	-48.8	-44.4	0	140	37	0	147.9	43.2
240	52	85.1	54.1	16	-46.3	-43.9	0	146.1	41.7	0	149.4	44.9
250	49.8	94.1	53.4	14.5	-41.4	-42.1	0	150.7	45.3	0	150.7	45.3
260	49.2	96.3	53.2	12.8	-41.6	-43.3	0	151.8	45.7	0	151.8	45.7

	M93 - NAM			D12 - EU		
0	0	0	0	0	0	0
10	43.5	119.6	1.3	-71.2	107	0.6
20	35.4	113.1	3.3	-66.4	156.9	1.5
30	38.5	107.3	5.3	-60.9	128.1	1.9
40	47	109.8	7.6	-53.3	88.9	2.8
50	46.8	112.6	11.2	-35.1	25.8	2.8
60	46	116.4	15.1	-29.5	-1.3	5.2
70	46.8	119.6	19.3	-50.3	18.8	5.2
80	53.3	117.2	24.5	-0.7	115.7	3.5
90	57.4	104.4	28.2	45.1	101.1	7.1
100	62.9	89.4	31.7	56.8	77.9	12.3
110	66.1	77	37.3	55.8	63.4	16.7
120	66.4	62.1	42.1	53.5	57.2	21
130	65.9	56.9	45.4			

Table S2: Relative plate motion (RPM) models [Torsvik et al., 2012] to transfer different APM models (Table S1) into the coordinates of stable Europe. Abbreviations: EU - stable Europe, NAM - North America, NWAF - Northwest Africa and SAF - South Africa.

	EU - NAM			NAM - NWAF			NWAF - SAF		
Age	Lat	Long	Ang	Lat	Long	Ang	Lat	Long	Ang
(Ma)	(°)	(°)	(°)	(°)	(°)	(°)	(°)	(°)	(°)
0	66.4	133	-1.2	80.9	22.8	1.3	0	0	0
10	66.4	133	-2.3	80.9	22.9	2.6	0	0	0
20	68.9	132.5	-5.1	80.6	24.4	5.5	0	0	0
30	68.3	131.7	-7	77.4	12.5	8.6	0	0	0
40	66.7	135.6	-9.2	74.5	-1.1	12.6	0	0	0
50	64.4	141	-11.7	75.9	-3.5	16.2	0	0	0
60	55.6	145.8	-14.1	81.6	5.1	19.1	0	0	0
70	55.7	147.1	-16.2	81.6	-6.5	22.4	0	0	0
80	64.1	148	-18.7	78.2	-18.8	27.5	0	0	0
90	66.6	149.9	-20.2	74.3	-22.7	33.9	0	0	0
100	66.8	151.6	-21.1	69.4	-23.5	40.5	0	0	0
110	67.7	153.3	-22.1	67.5	-22.1	47.5	0	0	0
120	69	154.7	-23.1	66	-20.6	54.2	0	0	0
130	69	154.8	-23	66	-19.2	57.7	33.7	26	2
140	69	154.8	-23.1	66.4	-18.2	60.1	33.6	26	2.3
150	69	154.8	-23.1	66.4	-17.8	63.2	33.6	26	2.3
160	69	154.8	-23.3	67.1	-15.1	66.6	33.6	26	2.3
170	69	154.8	-23.5	67.1	-13.9	70.6	33.6	26	2.3
180	69	154.8	-23.6	65.9	-14.5	73.1	33.6	26	2.3
190	69	154.8	-23.6	64.8	-15	75.8	33.6	26	2.3
200	80.6	156.2	-31.5	64.3	-15	77.4	33.6	26	2.3
210	76	159	-28.5	64.3	-14.7	78	33.6	26	2.3
220	78.6	161.9	-31	64.3	-14.7	78	33.6	26	2.3
230	78.6	161.9	-31	64.3	-14.7	78	33.6	26	2.3
240	78.6	161.9	-31	64.3	-14.7	78	33.6	26	2.3
250	78.6	161.9	-31	64.3	-14.7	78	33.6	26	2.3
260	78.6	161.9	-31	64.3	-14.7	78	33.6	26	2.3

Table S3: The selected high-quality paleomagnetic poles from the North China Block during the Middle Permian - Early Triassic. The numerical ages of the paleo-poles are assigned as midpoints of Period/Epoch in the geologic time scale of Gradstein et al. [2012]. If not presented in the source publications, A_{95} is recalculated using the formula $A_{95} = \sqrt{dm \times dp}$ [Khramov, 1987], where dm and dp are semi-major and semi-minor axes of error ellipses. All the clastic paleo-poles are corrected for the inclination errors (IE) using a common factor of 0.6, following the suggestions of Torsvik et al. [2012] and Van der Voo et al. [2015]. This common shallowing factor of 0.6, from which the Siberian (stable European) and later segments of NCA paleopoles are determined [Torsvik et al., 2012; Van der Voo et al., 2015], is adopted here to avoid reconstruction uncertainties due to different selections of the value. The quality of the paleo-poles is assessed by the widely accepted seven criteria [Van der Voo, 1990]: 1, adequate demagnetization and remanence components analysis; 2, field test (fold test, conglomerate test and bake test); 3, antipodal reversals; 4, firm statistical results with the number of samples no smaller than 24 and A_{95} no larger than 16°; 5, no large afterward localized rotations; 6, well-constrained age for the host rock; 7, no remagnetizations. Paleo-poles get a '1' for passing or a '0' for failing each criterion. A '-' is assigned if a criterion is not mentioned in the source paper.

Lithology, location	Age		Sites		Paleo-Poles (without IE corrections)			Paleo-Poles (with IE corrections)		Grading	Q	CM	Ref
		(Ma)	LonS (°E)	LatS (°N)	LonP (°E)	LatP (°N)	A95 (°)	LonP (°E)	LatP (°N)	1234567			
Early Triassic (T1)													
Redbeds; Shanxi	T1	249.7	111.9	37.6	4.8	50.3	4.8	20.2	55.8	1111-11	6		[Shi et al., 2004]
Sediments; Shanxi	T1	249.7	112	37.6	4.8	50.3	4.8	20.1	55.8	1111-11	6		[Huang et al., 2005]
Redbeds; Shaanxi	T1	249.7	110.2	35.5	348.3	61.9	3.8	8.8	67.8	1-11111	6		[Yang et al., 1991]
Redbeds; Shanxi	T1	249.7	110.8	36.3	356.3	64.8	3	25.9	69.8	111-1-11	6		[Tan et al., 1991]
Sandstone; Shanxi	T1	249.7	110.3	35.5	356.5	57.8	2.8	15.2	63.2	1111-11	6		[Ma et al., 1993]
Shale, mudstone; Shanxi	T1	249.7	112.3	37.8	351	50	6	360	55.1	1-11-11	5		[Embleton et al., 1996]
Middle (P2) and Late Permian (P3)													
Sanstone; Hebei and Shanxi	P3	256	113.2	38.7	356.9	47.1	15.5	6.3	52.3	1011111	6		[Zhao and Coe, 1989]
Redbeds; Gansu	P3	256	98	39.6	358.6	41	4.3	11.3	46.8	-1111-1	5		[Meng et al., 1989]
Redshale, mudstone; Shanxi	P3	256	112.3	37.8	357.4	47.8	4	7.5	53	1-11-11	5		[Embleton et al., 1996]
Mudstone, sandstone; Shaanxi	P2	266.1	110.3	35.5	358.7	49.5	3.4	10.4	54.4	1111-11	6		[Ma et al., 1993]
Redbeds; Shanxi	P2	266.1	112.3	37.8	357.8	44.3	5.2	5.6	48.8	1-11111	6		[McElhinny et al., 1981]
Sandstone, basalt; Inner Mongolia	P2	266.1	118.4	43.7	3.7	48.7	6.9	16.9	55.7	1111–1	5		[Zhao et al., 2013]

Table S4: The input APWPs of Siberia [Torsvik et al., 2012], stable Europe [Torsvik et al., 2012] and North China [Van der Voo et al., 2015] for the geometric parameterizations. See Methods for the detailed descriptions. N: number of paleopoles.

Siberia APWP					European APWP				North China APWP			
Age (Ma)	N	A95 (°)	Long (°E)	Lat (°N)	N	A95 (°)	Long (°E)	Lat (°N)	N	A95 (°)	Long (°E)	Lat (°N)
0	24	1.9	173.9	88.5	24	1.9	173.9	88.5	24	1.9	173.9	88.5
10	49	1.8	150	86.7	49	1.8	150	86.7	49	1.8	150	86.7
20	31	2.6	152.1	84.4	31	2.6	152.1	84.4	31	2.6	152.1	84.4
30	24	2.6	146.5	83.1	24	2.6	146.5	83.1	24	2.6	146.5	83.1
40	24	2.9	144.3	81.1	24	2.9	144.3	81.1	24	2.9	144.3	81.1
50	33	2.8	164.7	78.9	33	2.8	164.7	78.9	33	2.8	164.7	78.9
60	44	2.1	172.6	78.2	44	2.1	172.6	78.2	1	16	144.4	76.4
70	32	2.5	175.7	79.2	32	2.5	175.7	79.2	6	8	200	78.6
80	25	2.9	177.9	79.7	25	2.9	177.9	79.7	15	5.7	168.1	79.1
90	28	2.5	167.2	80.4	28	2.5	167.2	80.4	13	5.8	155.5	77.2
100	14	3.3	152.3	80.8	14	3.3	152.3	80.8	3	11.3	164.9	76.2
110	21	3.3	193.1	81.2	21	3.3	193.1	81.2	13	4.6	161.6	75.3
120	28	2.6	190.1	79	28	2.6	190.1	79	20	4.1	162.5	78
130	18	2.8	183.4	75	18	2.8	183.4	75	9	6.6	168	81.1
140	9	6	187.9	72.4	9	6	187.9	72.4	-	16	174.4	76.8
150	15	6.4	154.2	72.9	15	6.4	154.2	72.9	10	5.1	177	72.3
160	19	5.1	143.4	70.5	19	5.1	143.4	70.5	14	4.7	174.3	74.7
170	18	4.6	136.4	67.3	18	4.6	136.4	67.3	5	9.6	160.7	78
180	33	3.4	113.9	68.3	33	3.4	113.9	68.3	2	3.3	106	84.2
190	46	2.9	98.8	64.1	46	2.9	98.8	64.1	2	3.3	106	84.2
200	39	2.8	99.3	57.9	39	2.8	99.3	57.9	-	16	77.7	75.8
210	41	2.2	110.8	56.1	41	2.2	110.8	56.1	2	16	42.1	68.4
220	35	2.3	124.1	52.8	35	2.3	124.1	52.8	2	16	42.1	68.4
230	33	2.5	132.1	50.7	33	2.5	132.1	50.7	-	16	41.8	65.9
240	31	3.6	141.5	52.2	31	3.6	141.5	52.2	6	6.6	14.6	61.5
250	5	5.8	146.2	56.1	34	3.6	149.2	53.4	9	5.5	12.1	57.9
260	4	7.9	156.2	54.2	35	2.6	150.5	53.8	6	3.5	9.6	51.9

Table S5: Comparison of great circle (GC) and small circle (SC) fits to the identified APWP tracks (Figure 1). SC fit provides a significant improvement over a GC fit to an APWP track when the variance ratio (V_r) is larger than the critical value ($F_{1,n-3}$) at the confidence level of 95%. Two alternative sets of stage rotations are then calculated: one is exclusively derived from GC fits; another results from a combination of GC and SC fits based on the comparison between V_r and $F_{1,n-3}$.

			GC fits				SC fits							Stage rotations (GC)			Stage rotations (GC+SC)		
APWP Track	Interval	N	Long (°E)	Lat (°N)	Radius (°)	Angle (°)	Long (°E)	Lat (°N)	Radius (°)	Angle (°)	V_r	$F_{1,n-3}$	Better fit	Long (°E)	Lat (°N)	Angle (°)	Long (°E)	Lat (°N)	Angle (°)
EuSib-1	0-40	5	49.9	0.8	90.0	-7.6	64.2	70.6	19.8	-22.5	0.0	18.5	GC	49.9	0.8	-7.6	49.9	0.8	-7.6
EuSib-2	40-60	3	127.6	-8.6	90.0	-5.8	-161.2	84.5	7.2	47.0	0.0	–	GC	127.8	-1.2	-5.8	127.8	-1.2	-5.8
EuSib-3	60-110	6	172.1	-9.9	90.0	-3.0	173.1	82.4	3.2	78.6	9.0	10.1	GC	171.7	0.6	-3.0	171.7	0.6	-3.0
EuSib-4	110-140	4	270.0	-1.8	90.0	8.9	-141.6	73.4	9.1	58.1	1.3	161.4	GC	269.2	-0.1	8.9	269.2	-0.1	8.9
EuSib-5	140-170	4	177.0	-16.8	90.0	17.8	169.4	50.4	23.4	45.8	834.4	161.4	SC	176.8	2.8	17.8	156.3	68.9	45.8
EuSib-6	170-200	4	145.3	-20.8	90.0	19.1	121.0	57.5	11.9	108.1	16.6	161.4	GC	146.6	3.7	19.1	104.4	3.0	19.1
EuSib-7	200-230	4	91.1	-32.1	90.0	-20.2	-121.3	71.5	47.4	27.5	9.3	161.4	GC	97.4	0.2	-20.2	55.2	-1.4	-20.2
Eub-8	230-260	4	160.0	-36.0	90.0	-11.6	112.3	76.1	26.6	26.2	5.3	161.4	GC	153.4	1.1	-11.6	111.2	0.6	-11.6
Sib-8	230-260	4	164.1	-34.6	90.0	-15.0	151.1	30.9	24.0	-37.5	0.2	161.4	GC	157.0	1.4	-15.0	114.8	1.0	-15.0
NCB-1	0-40	5	49.9	0.8	90.0	-7.6	64.2	70.6	19.8	-22.5	0.0	18.5	GC	49.9	0.8	-7.6	49.9	0.8	-7.6
NCB-2	40-80	5	174.7	-10.3	90.0	-3.2	-5.3	10.1	90.2	3.2	0.0	18.5	GC	174.3	-4.0	-3.2	174.3	-4.0	-3.2
NCB-3	80-110	4	53.4	4.3	90.0	-4.1	162.9	77.5	1.8	-156.5	7.4	161.4	GC	52.8	2.0	-4.1	52.8	2.0	-4.1
NCB-4	110-130	3	62.1	2.4	90.0	5.9	-155.9	71.6	12.3	-28.0	0.0	–	GC	61.7	1.7	5.9	61.7	1.7	5.9
NCB-5	130-150	3	95.5	-2.7	90.0	-9.0	116.1	56.0	29.2	-18.5	0.0	–	GC	95.3	-0.9	-9.0	95.3	-0.9	-9.0
NCB-6	150-200	6	116.6	-8.0	90.0	24.2	124.4	64.8	19.0	79.7	7.1	10.1	GC	117.0	-1.6	24.2	117.0	-1.6	24.2
NCB-7	200-230	4	97.4	-13.2	90.0	14.9	70.3	64.0	12.1	76.8	2389.6	161.4	SC	97.5	-2.9	14.9	89.6	76.9	76.8
NCB-8	230-260	4	66.7	-20.8	90.0	21.4	36.3	49.2	17.0	78.6	51.2	161.4	GC	67.4	0.5	21.4	352.0	7.0	21.4

Table S6: Stage Euler rotation parameters derived from the identified APWP tracks (Figure 1). Error ellipses are characterized using semi-major axis (Maj), semi-minor axis (Min) and the angle between meridians and the right-hand semi-major axis (Az).

Euler Rotation Parameters										
		Poles to Tracks		Stage Rotations			Error Ellipses			
Track	Period (Ma)	Long (°E)	Lat (°N)	Long (°E)	Lat (°N)	Angle (°)	Maj (°)	Min (°)	Az (°)	Fit method
Siberia & Stable Europe										
EuSib-1	0-40	49.9	0.8	49.9	0.8	-7.6	22	0.9	-85.2	GC
EuSib-2	40-60	127.6	-8.6	127.8	-1.2	-5.8	31	1.7	-89.2	GC
EuSib-3	60-110	172.1	-9.9	171.7	0.6	-3	380.8	2.1	90	GC
EuSib-4	110-140	270	-1.8	269.2	-0.1	8.9	33.3	3.7	-88.1	GC
EuSib-5	140-170	177	-16.8	176.8	2.8	17.8	405.3	5	89.9	GC
EuSib-6	170-200	145.3	-20.8	146.6	3.7	19.1	13.8	4.8	89.4	GC
EuSib-7	200-230	91.1	-32.1	97.4	0.2	-20.2	6.7	4.3	89.9	GC
Eu-8	230-260	160	-36	153.4	1.1	-11.6	86.5	5.4	-89.9	GC
Sib-8	230-260	164.1	-34.6	157	1.4	-15	13.1	5.1	-86.1	GC
North China										
NCB-1	0-40	49.9	0.8	49.9	0.8	-7.6	22	0.9	-85.2	GC
NCB-2	40-80	174.7	-10.3	174.3	-4	-3.2	399.4	3.3	89.9	GC
NCB-3	80-110	53.4	4.3	52.8	2	-4.1	119.2	4.9	-85.6	GC
NCB-4	110-130	62.1	2.4	61.7	1.7	5.9	73.2	6.9	-86.9	GC
NCB-5	130-150	95.5	-2.7	95.3	-0.9	-9	76.6	8.2	-83.7	GC
NCB-6	150-200	116.6	-8	117	-1.6	24.2	24	9	88	GC
NCB-7	200-230	97.4	-13.2	97.5	-2.9	14.9	74.5	11.3	-88.2	GC
NCB-8	230-260	66.7	-20.8	67.4	0.5	21.4	38.3	14.8	-83.8	GC

Table S7: TPW corrected APWPs of Siberia and North China. The finite rotations for TPW effects are from Torsvik et al. [2012, their Table 12].

	Siberia			North China		
Age	Lon	Lat	A_{95}	Lon	Lat	A_{95}
(Ma)	(^oE)	(^oN)	(^{o})	(^oE)	(^oN)	(^{o})
0	173.9	88.5	1.9	173.9	88.5	1.9
10	150.0	86.7	1.8	150.0	86.7	1.8
20	152.1	84.4	2.6	152.1	84.4	2.6
30	146.5	83.1	2.6	146.5	83.1	2.6
40	144.3	81.1	2.9	144.3	81.1	2.9
50	164.7	78.9	2.8	164.7	78.9	2.8
60	172.6	78.2	2.1	144.4	76.4	6.4
70	175.7	79.2	2.5	200.0	78.6	8
80	177.9	79.7	2.9	168.1	79.1	5.7
90	167.2	80.4	2.5	155.5	77.2	5.8
100	152.3	80.8	3.3	164.9	76.2	11.3
110	150.2	78.3	3.3	141.6	70.1	4.6
120	154.8	76.3	2.6	138.9	72.7	4.1
130	157.7	72.1	2.8	136.8	75.9	6.6
140	164.8	70.3	6.0	148.6	72.8	16.0
150	154.2	72.9	6.4	177.0	72.3	5.1
160	153.6	73.6	5.1	191.0	75.4	4.7
170	154.3	73.8	4.6	206.4	79.3	9.6
180	132.7	81.0	3.4	277.2	82.3	3.3
190	94.0	82.1	2.9	278.6	77.8	3.3
200	95.6	80.4	2.8	311.7	79.0	16.0
210	120.6	73.6	2.2	352.3	70.6	16.0
220	134.8	64.7	2.3	5.2	71.5	16.0
230	139.3	58.1	2.5	21.3	69.2	16.0
240	145.7	55.5	3.6	6.3	61.5	6.6
250	146.2	56.1	5.8	12.1	57.9	5.5
260	156.2	54.2	7.9	9.6	51.9	3.5

Table S8: Circle fits to the TPW corrected APWPs of Siberia and North China.

APWP track	Interval	N	GC poles				SC poles				Statistics			Stage rotations		
			Long (^oE)	Lat (^oN)	Angle (^{o})	Radius (^{o})	Long (^oE)	Lat (^oN)	Angle (^{o})	Radius (^{o})	V_r	$F_{1,n-3}$	Fit	Long (^oE)	Lat (^oN)	Angle (^{o})
Sib-1	0-40	5	49.9	0.8	-7.6	90	64.2	70.6	-22.5	19.8	0	18.5	GC	49.9	0.8	-7.6
Sib-2	40-60	3	127.6	-8.6	-5.8	90	-161.2	84.5	47	7.2	0	–	GC	127.8	-1.2	-5.8
Sib-3	60-110	6	160	-10.3	-4.5	90	162.2	78.8	165.8	2.5	14.3	10.1	GC*	159.8	-0.1	-4.5
Sib-4	110-140	4	90	-6	-8.9	90	-169.8	75.3	58.1	9.1	1.3	161.4	GC	90.8	-8.8	-8.9
Sib-5	140-170	4	114.3	-12.9	4.7	90	163.5	73.1	-118.6	2.8	18.1	161.4	GC	115.8	-6.7	4.7
Sib-6	170-200	4	97	-8.4	13.8	90	113.8	67.4	59.1	14.5	1.4	161.4	GC	98.1	-7.1	13.8
Sib-7	200-230	4	62.9	-8.4	-25.7	90	-125.5	30.8	28	66.7	1.1	161.4	GC	64.1	-8.9	-25.7
Sib-8	230-260	4	122.4	-31.4	-10.2	90	158.6	66.1	50.6	12	5.1	161.4	GC	124.4	-6.9	-10.2
NCB-1	0-40	5	49.9	0.8	-7.6	90	64.2	70.6	-22.5	19.8	0	18.5	GC	49.9	0.8	-7.6
NCB-2	40-80	5	174.7	-10.3	-3.2	90	-5.3	10.1	3.2	90.2	0	18.5	GC	174.3	-4	-3.2
NCB-3	80-110	4	204.9	-9.3	11.2	90	-164.3	29.2	14.4	50.6	0	161.4	GC	204.1	-4.4	11.2
NCB-4	110-130	3	62.1	-3.9	5.9	90	179.8	71.7	-28	12.3	0	–	GC	63.4	1.8	5.9
NCB-5	130-150	3	142.9	-15.3	-11.3	90	164.2	77.9	122.7	6.5	0	–	GC	143.3	-5.4	-11.3
NCB-6	150-200	6	67.6	7.4	26.5	90	78.4	73	64.2	25.9	1.8	10.1	GC	65.7	2.8	26.5
NCB-7	200-230	4	318.1	-12.5	-19.8	90	22.6	81.2	114	11.7	7.8	161.4	GC	314.9	3.3	-19.8
NCB-8	230-260	4	269.2	7	-18.1	90	40.4	53.5	60.2	18.2	0.8	161.4	GC	262.6	0.8	-18.1

* The great circle approached is preferred because the small circle fit predicts unrealistically large rotation rates during the interval.

Table S9: Finite rotations of Siberia and NCA that are calculated from their TPW corrected APWPs (Table S7). To quantify the differences between the TPW corrected finite rotations and their counterparts in Table 1, the great circle distances (GCDs) are calculated in the coordinates of the reference site [112^oE, 51^oN] that is located in the middle of the suture zone.

	Finite Rotations - Siberia				Finite Rotations - NCA			
Age (Ma)	Lon (^oE)	Lat (^oN)	Angle (^{o})	GCD (^{o})	Lon (^oE)	Lat (^oN)	Angle (^{o})	GCD (^{o})
0	0.0	0.0	0.0	0.0	0.0	0.0	0.0	0.0
10	48.1	0.9	2.1	0.0	48.1	0.9	2.1	0.0
20	51.3	0.7	4.1	0.0	51.3	0.7	4.1	0.0
30	49.8	0.8	5.6	0.0	49.8	0.8	5.6	0.0
40	49.5	0.8	7.7	0.0	49.5	0.8	7.7	0.0
50	73.5	-1.3	9.5	0.0	62.6	-1.2	7.1	0.0
60	82.9	-2.2	10.5	0.0	35.2	2.6	10.4	0.0
70	87.0	-2.6	10.5	0.0	118.2	-7.4	7.8	0.0
80	89.7	-2.9	10.5	0.0	68.0	-2.0	6.9	0.0
90	80.1	-2.1	9.9	0.3	57.9	0.6	8.8	0.8
100	67.3	-1.0	9.6	0.8	65.3	-0.7	7.7	1.3
110	57.5	0.1	10.5	2.8	42.7	3.7	15.8	0.4
120	62.8	-2.0	12.4	9.1	37.7	4.7	13.7	0.6
130	66.3	-4.1	16.7	9.4	30.8	6.2	10.7	0.8
140	73.5	-5.7	18.3	9.5	41.1	4.4	11.5	2.5
150	60.6	-2.9	15.9	9.0	86.9	-3.7	12.1	0.7
160	60.3	-2.6	15.4	9.0	113.3	-10.5	8.7	1.3
170	61.2	-2.7	15.3	9.0	150.1	-17.9	6.4	0.8
180	34.5	6.9	8.8	8.6	219.2	-14.3	11.1	1.6
190	356.1	14.9	8.8	9.5	220.2	-11.1	15.8	0.7
200	1.1	11.5	10.2	9.9	231.3	-12.0	15.5	4.1
210	28.6	0.5	15.7	9.3	256.2	-8.9	24.4	8.7
220	42.1	-5.1	24.2	8.5	267.4	-10.2	23.7	7.7
230	46.7	-7.0	30.7	8.5	281.2	-11.0	25.9	6.5
240	53.3	-9.4	31.8	9.0	273.0	-5.7	36.7	8.3
250	53.7	-9.5	31.8	10.7	274.8	-5.9	37.9	9.3
260	63.2	-12.7	34.4	8.7	273.4	-4.4	44.0	8.3

Table S10: Age-depth relationship for tomography slices [van der Meer et al., 2010].

Age (Ma)	Depth (km)
120	1325
130	1506
140	1700
150	1819
160	1900
170	1995
180	2100
190	2203
200	2300
210	2392
220	2480
230	2566
240	2650
250	2733
260	2815

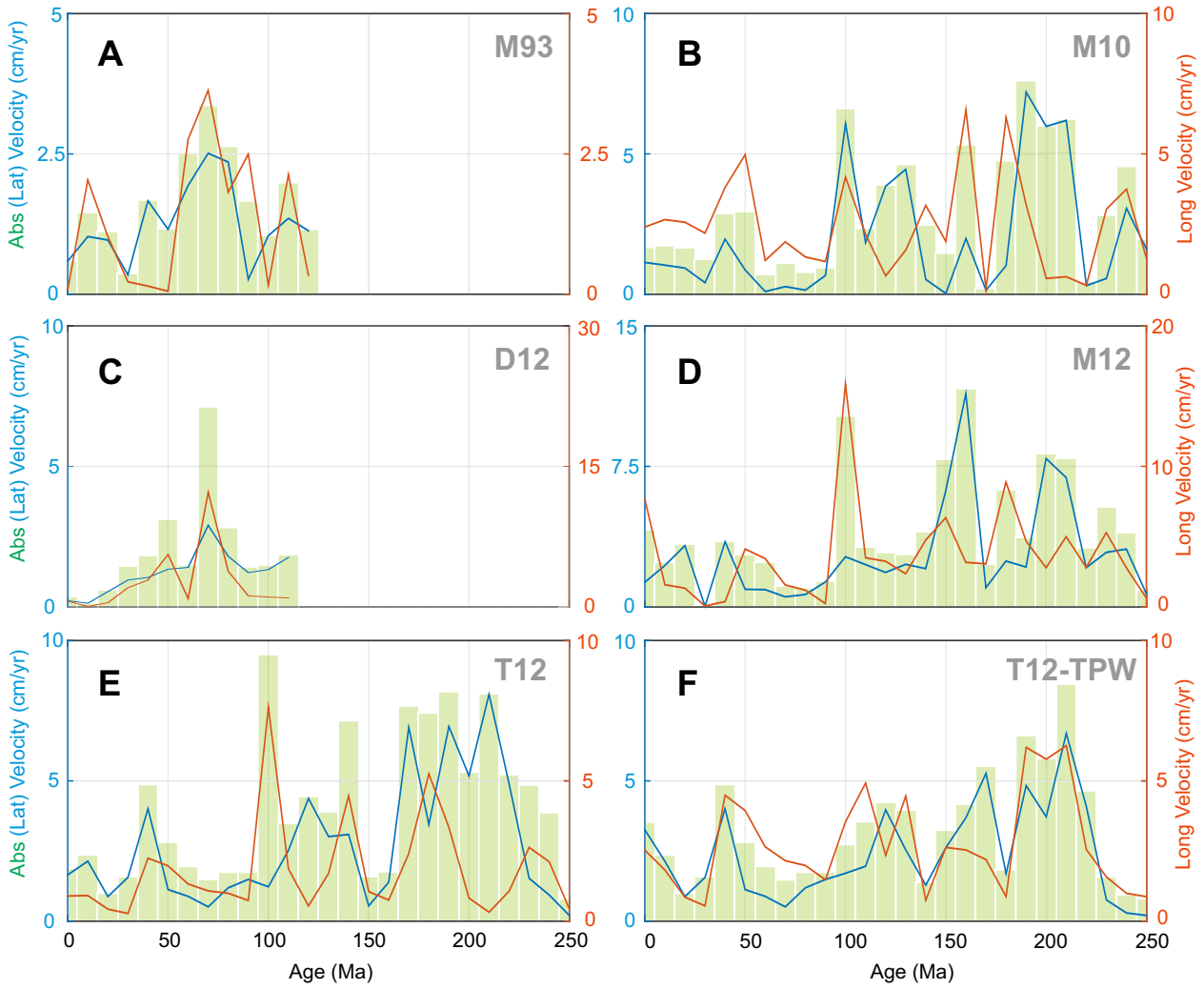

Figure S1: Absolute velocity predictions from different APM models: M93 [Müller et al., 1993], D12 [Doubrovine et al., 2012], M10 [van der Meer et al., 2010], M12 [Mitchell et al., 2012], T12 [Torsvik et al., 2012], and T12-TPW [Torsvik et al., 2012]. Absolute velocities are indicated by the green bars, and the two orthogonal velocity components are shown as the blue and orange lines.

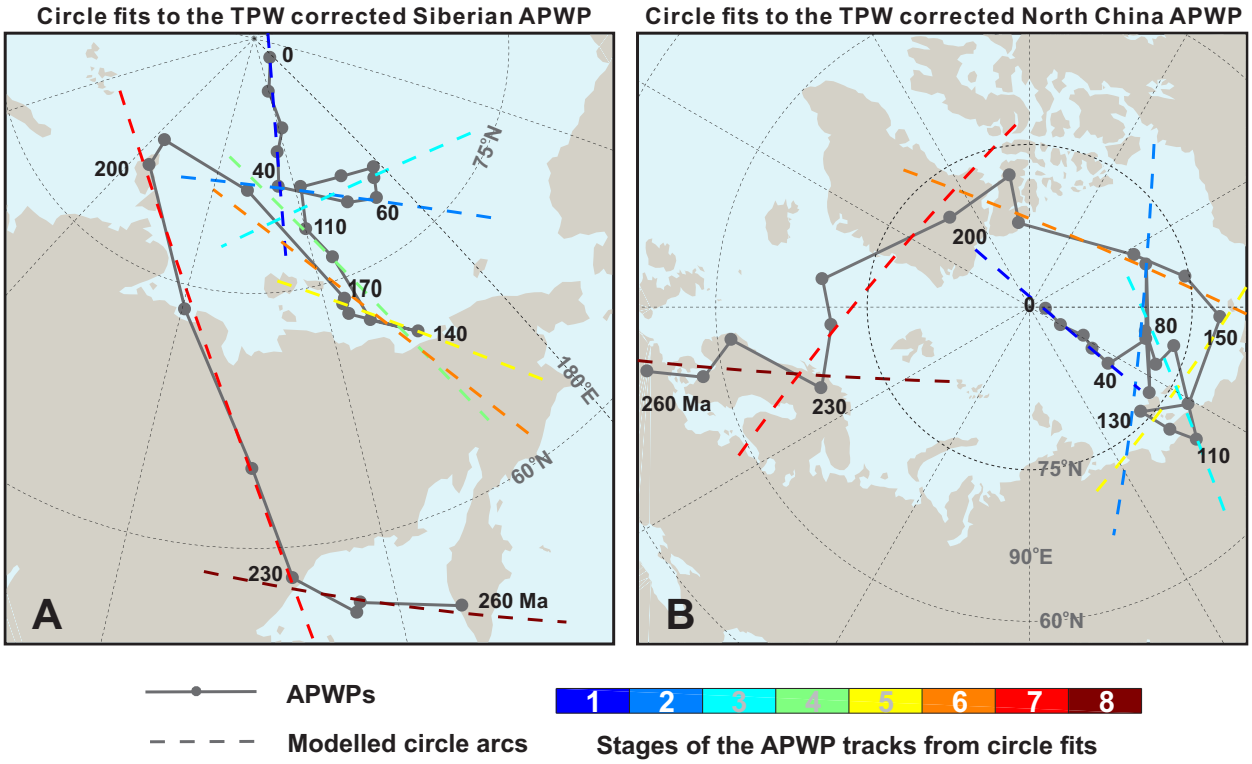

Figure S2: Circle fits to the TPW corrected APWPs of Siberia (A) and North China (B) (Table S7). Errors in the APWPs are not shown for clarity. The results of the circle fits are shown in Table S8.

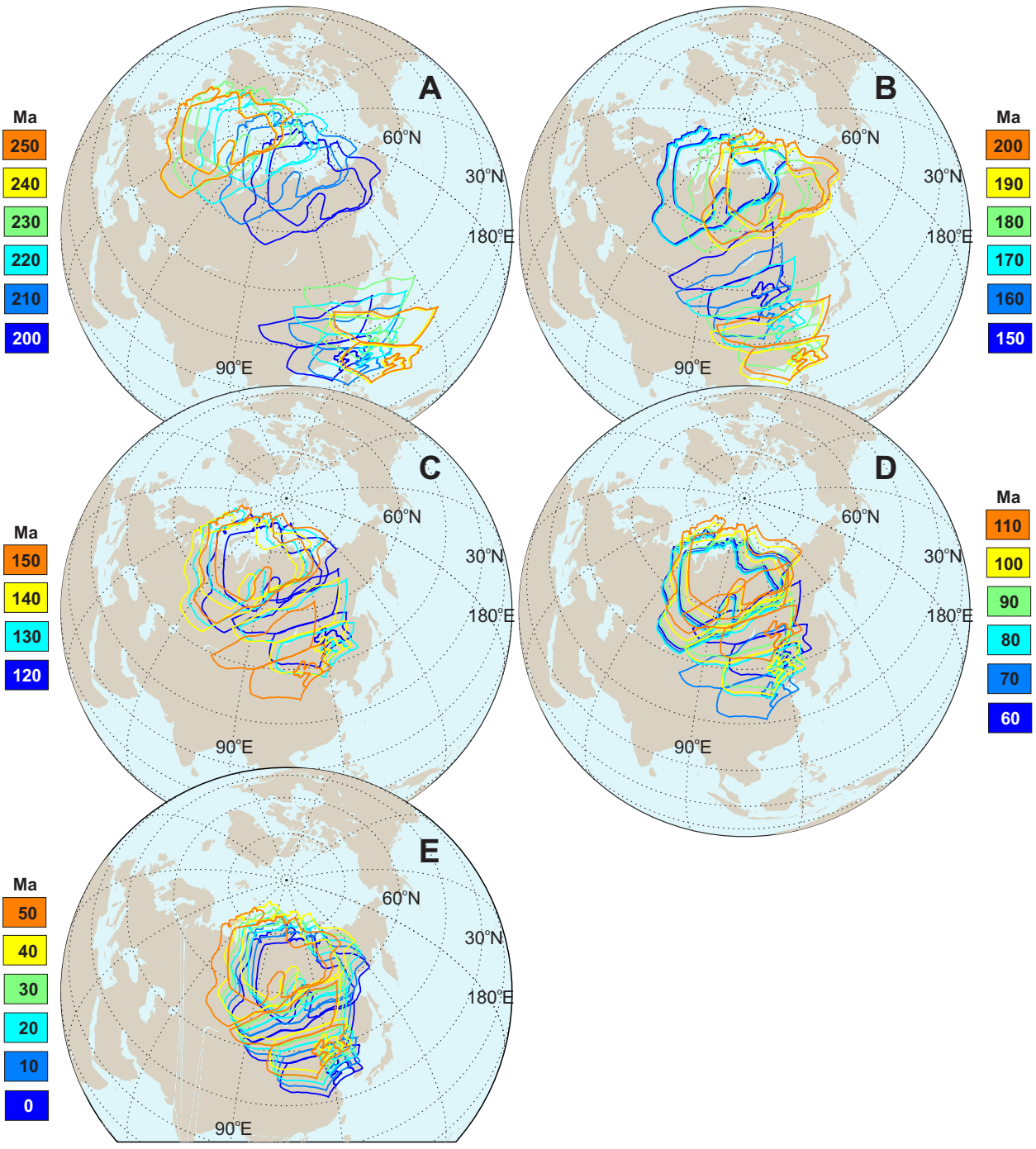

Figure S3: Reconstructions of Siberia and NCA over the last 250 Ma from their TPW corrected APWPs (Figure S2). The finite rotations are shown in Table S9. The post-suturing anomalous reconstructions at the interval of 110-60 Ma are not adjusted so the reader has a complete sense of the robustness of our method.

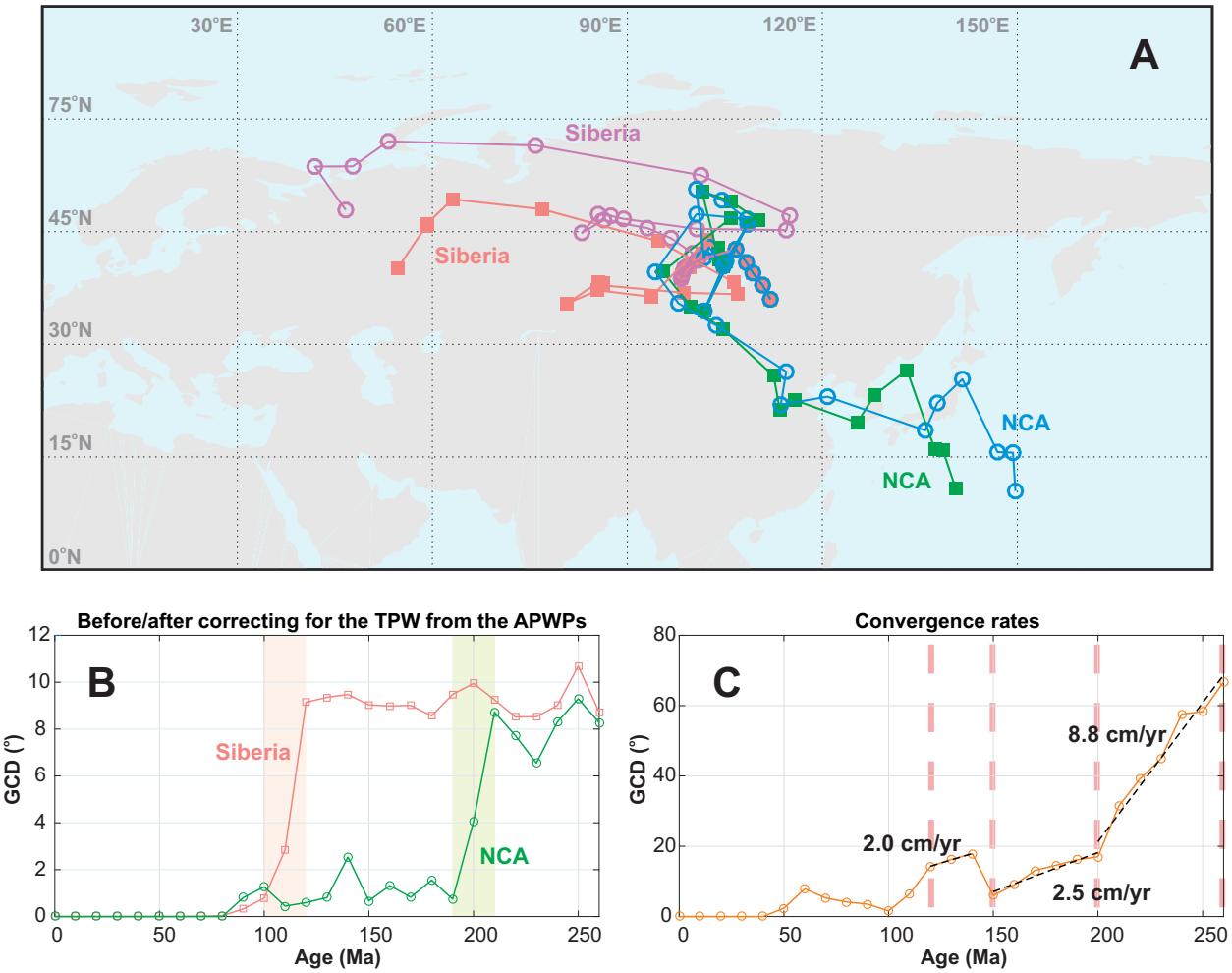

Figure S4: A comparison of the reconstructions both from the TPW corrected APWPs (Table S9) and from the TPW corrected APMs (Table 1). (A) Filled symbols denote the reconstructions from the TPW corrected APWPs; open symbols represent the reconstructions from the TPW corrected APMs. The reconstructions are illustrated in the coordinates of a reference site [112.0°E, 51.0°N] that is located in the middle of the suture zone. (B) Great circle distances (GCDs) between the reconstructions both from the TPW corrected APWPs and from the TPW corrected APMs. The pink (green) shading highlights the interval when there is a significant increase in the GCDs between the restorations of Siberia (NCA) from the two approaches. (C) GCDs between the suture margins (orange symbols and line) and associated convergence rates between 260 Ma and 120 Ma (black dashed lines).

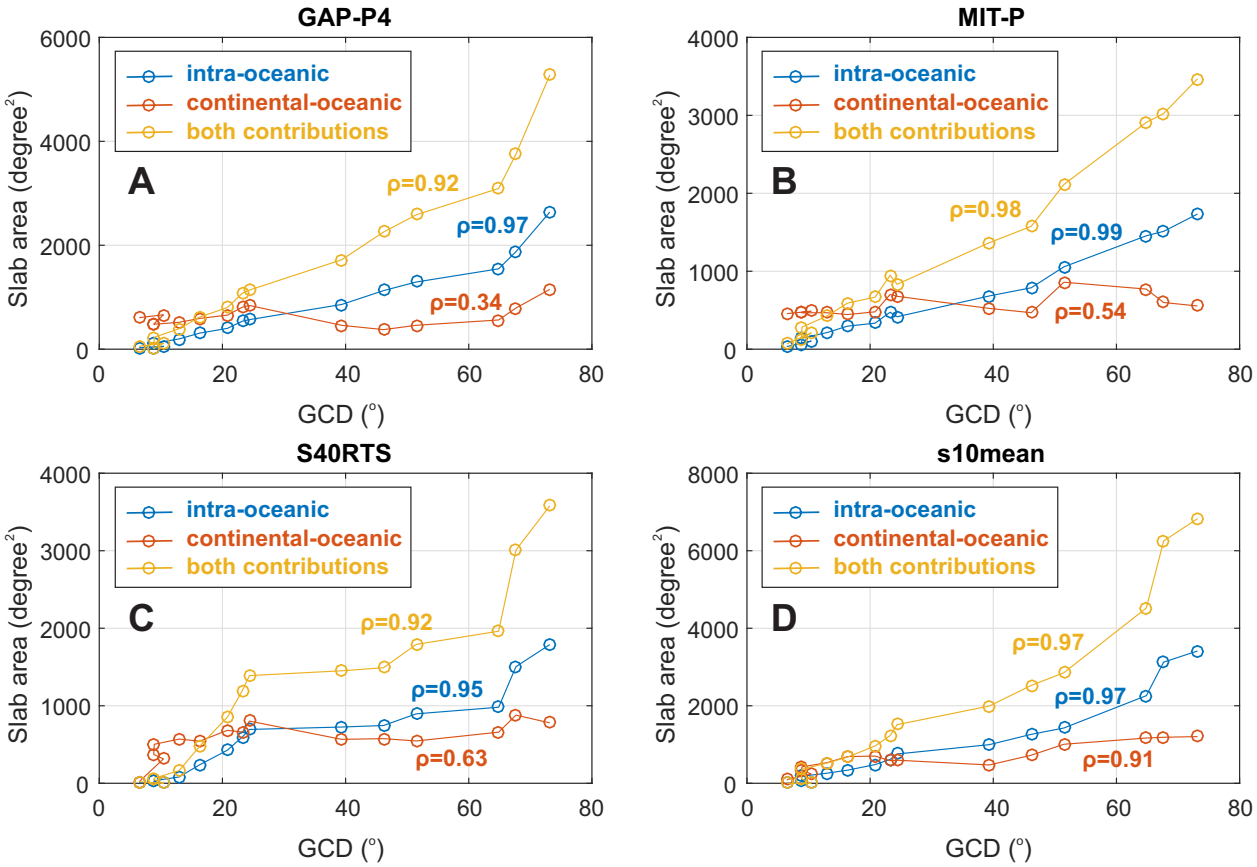

Figure S5: The Pearson correlation coefficients (ρ) between the great circle distances (GCDs) between the two suture margins and area of slabs associated with different types of subduction according to different tomographic models.

References

Cox, A. and Hart, R. B. (1986). Plate Tectonics: How It Works.

Doubrovine, P. V., Steinberger, B., and Torsvik, T. H. (2012). Absolute plate motions in a reference frame defined by moving hot spots in the Pacific, Atlantic, and Indian oceans. *Journal of Geophysical Research: Solid Earth*, 117(B9).

Embleton, B. J., McElhinny, M. W., Ma, X., Zhang, Z., and Li, Z. X. (1996). Permo-Triassic magnetostratigraphy in China: the type section near Taiyuan, Shanxi province, North China. *Geophysical Journal International*, 126(2):382–388.

Fisher, N. I., Lewis, T., and Embleton, B. J. (1987). *Statistical analysis of spherical data*. Cambridge University Press.

Gradstein, F. M., Ogg, J. G., and Schmitz, M. (2012). *The Geologic Time Scale 2012, 2-volume set*. Elsevier.

Gray, N. H., Geiser, P. A., and Geiser, J. R. (1980). On the least-squares fit of small and great circles to spherically projected orientation data. *Journal of the International Association for Mathematical Geology*, 12(3):173–184.

Huang, B., Shi, R., Wang, Y., and Zhu, R. (2005). Palaeomagnetic investigation on EarlyCMiddle Triassic sediments of the North China block: a new Early Triassic palaeopole and its tectonic implications. *Geophysical Journal International*, 160(1):101–113.

Khramov, A. N. (1987). *Paleomagnetology*. Springer–Verlag, Berlin.

Ma, X., Xing, L., Yang, Z., Xu, S., and Zhang, J. (1993). Palaeomagnetic study since Late Paleozoic in the Ordos Basin. *Chinese Journal of Geophysics*, 36(1):68–79.

McElhinny, M., Embleton, B., Ma, X., and Zhang, Z. (1981). Fragmentation of Asia in the Permian. *Nature*, 293:212–216.

Meng, Z., Coe, R., and Frost, G. (1989). Paleomagnetic Results From Late Permian Redbeds in Gansu Province, China. *Eos Trans. AGU*, 70:1070.

Mitchell, R. N., Kilian, T. M., and Evans, D. A. (2012). Supercontinent cycles and the calculation of absolute palaeolongitude in deep time. *Nature*, 482(7384):208–211.

Müller, R. D., Royer, J.-Y., and Lawver, L. A. (1993). Revised plate motions relative to the hotspots from combined Atlantic and Indian Ocean hotspot tracks. *Geology*, 21(3):275–278.

Shi, R., Huang, B., Zhu, R., and Ren, S. (2004). Paleomagnetic study on the Early Triassic red beds from Jiaocheng, Shanxi Province. *Science in China Series D: Earth Sciences*, 47(2):108–114.

Smirnov, A. V. and Tarduno, J. A. (2010). Co-location of eruption sites of the Siberian Traps and North Atlantic Igneous Province: Implications for the nature of hotspots and mantle plumes. *Earth and Planetary Science Letters*, 297(3):687–690.

Steinberger, B. and Torsvik, T. (2010). Toward an explanation for the present and past locations of the poles. *Geochemistry, Geophysics, Geosystems*, 11(6).

Tan, X., Fang, D., Yuan, Y., Fan, S., and Bao, J. (1991). Paleomagnetic study on red beds, Liujiaogou Formation (TRL) from Taoyuan, Yaoqu, Jixian, Shanxi Province. *Acta Geophysica Sinica*, 34(6):736–743.

Torsvik, T. H., der Voo, R. V., Preeden, U., Niocaill, C. M., Steinberger, B., Doubrovine, P. V., van Hinsbergen, D. J., Domeier, M., Gaina, C., Tohver, E., Meert, J. G., McCausland, P. J., and Cocks, L. R. M. (2012). Phanerozoic polar wander, palaeogeography and dynamics. *Earth-Science Reviews*, 114(3–4):325–368.

van der Meer, D. G., Spakman, W., van Hinsbergen, D. J., Amaru, M. L., and Torsvik, T. H. (2010). Towards absolute plate motions constrained by lower-mantle slab remnants. *Nature Geoscience*, 3(1):36–40.

Van der Voo, R. (1990). Phanerozoic paleomagnetic poles from Europe and North America and comparisons with continental reconstructions. *Reviews of Geophysics*, 28(2):167–206.

Van der Voo, R., Van Hinsbergen, D. J., Domeier, M., Spakman, W., and Torsvik, T. H. (2015). Latest Jurassic–earliest Cretaceous closure of the Mongol–Okhotsk Ocean: a paleomagnetic and seismological–tomographic analysis. In *Late Jurassic Margin of LaurasiałA Record of Faulting Accommodating Plate Rotation*, volume 513.

Wu, L. and Kravchinsky, V. A. (2014). Derivation of paleolongitude from the geometric parametrization of apparent polar wander path: Implication for absolute plate motion reconstruction. *Geophysical Research Letters*, 41(13):4503–4511.

Wu, L., Kravchinsky, V. A., and Potter, D. K. (2015). PMTec: A new MATLAB toolbox for absolute plate motion reconstructions from paleomagnetism. *Computers & Geosciences*, 82:139–151.

Yang, Z., Ma, X., Besse, J., Courtillot, V., Xing, L., Xu, S., and Zhang, J. (1991). Paleomagnetic results from Triassic sections in the Ordos Basin, North China. *Earth and Planetary Science Letters*, 104(2–4):258–277.

Zhao, P., Chen, Y., Xu, B., Faure, M., Shi, G., and Choulet, F. (2013). Did the Paleo-Asian Ocean between North China Block and Mongolia Block exist during the late Paleozoic? First paleomagnetic evidence from central-eastern Inner Mongolia, China. *Journal of Geophysical Research: Solid Earth*, 118(5):1873–1894.

Zhao, X. and Coe, R. S. (1989). Tectonic implications of Perm-Triassic paleomagnetic results from north and south China. *Geophysical Monograph Series*, 50:267–283.